Progressive mural cell deficiencies across the lifespan in a *foxf2* model of Cerebral Small Vessel Disease

Merry Faye E. Graff[1,3], Emma E.M. Heeg[1,3], David A. Elliott[2], and Sarah J. Childs[1,3]*

[1] Alberta Children's Hospital Research Institute, University of Calgary, T2N 4N1, Canada.

[2] Hotchkiss Brain Institute Advanced Microscopy Platform, University of Calgary, T2N 4N1, Canada

[3] Department of Biochemistry and Molecular Biology, University of Calgary, T2N 4N1, Canada.

*Corresponding author email: schilds@ucalgary.ca.

Sarah Childs ORCID iD: https://orcid.org/0000-0003-2261-580X.
Merry Faye Graff ORCID iD: https://orcid.org/0009-0006-6861-5759
Emma Heeg ORCID iD: https://orcid.org/0009-0002-0879-133X
David Elliott ORCID iD: https://orcid.org/0009-0005-5548-5572

Keywords: Foxf2, Pericytes, Mural Cells, Zebrafish, Vascular Stability, Small Vessel Disease

Abstract (250 words)

Cerebral Small Vessel Disease (SVD) is a leading cause of stroke and dementia and yet is often an incidental finding in aged patients due to the inaccessibility of brain vasculature to imaging. Animal models are important for modelling the development and progression of SVD across the lifespan. In humans, reduced *FOXF2* is associated with an increased stroke risk and SVD prevalence in humans. In the zebrafish, *foxf2* is expressed in pericytes and vascular smooth muscle cells and is involved in vascular stability. We use partial *foxf2* loss of function (*foxf2a*$^{-/-}$) to model the lifespan effect of reduced Foxf2 on small vessel biology. We find that the initial pool of pericytes in developing *foxf2a* mutants is strongly reduced. The few brain pericytes present in mutants have strikingly longer processes and enlarged soma. *foxf2a* mutant pericytes can partially repopulate the brain after ablation suggesting some recovery is possible. Despite this capacity, adult *foxf2a* mutant brains show regional heterogeneity, with some areas of normality and others with severe pericyte depletion. Taken together, *foxf2a* mutants fail to generate a sufficient initial population of pericytes. The pericytes that remain have abnormal cell morphology. Over the lifespan, initial pericyte deficits are not repaired and lead to severely abnormal cerebrovasculature in adults. This work opens new avenues for modeling progressive genetic forms of human Cerebral Small Vessel Disease.

Introduction

Brain microvessels supply billions of neurons and other brain cells with the oxygen and nutrients they need. Pathologies affecting brain microvasculature progress slowly and silently over a lifetime but have devastating consequences from decreased perfusion and vascular destabilization. Cerebral small vessel disease (CSVD) encompasses progressive heterogeneous changes in brain microvessels; it is the most common cause of vascular dementia and a significant contributor to stroke and cognitive decline (Østergaard et al., 2016). 25% of all strokes are the result of CSVD, yet effective targeted treatments remain elusive (Østergaard et al., 2016). This is in part due to the inability to both detect and assess progressive damage in the brain.

While there are several genes implicated in familial CSVD (i.e., *NOTCH3*, *HTRA1*, *FOXC1*, *COL4A1* and *COL4A2*), there is a lack of suitable *in vivo* models for studying disease development and progression. Research has predominantly focused on *NOTCH3*, but over the last decade, *FOXF2* has emerged as a risk locus for CSVD (Chauhan et al., 2016; Duperron et al., 2023). SNPs in the intergenic region between *FOXF2* and *FOXQ1* decrease *FOXF2* expression and significantly increase stroke risk due to the variant decreasing the efficiency of *ETS1* binding to a novel *FOXF2* enhancer (Ryu et al., 2022).

Foxf2 promotes mural cell differentiation and vascular stability in the zebrafish brain and is expressed highly in brain pericytes (Ahuja et al., 2024; Chauhan et al., 2016; Reyahi et al., 2015; Ryu et al., 2022). Brain pericytes interact closely with endothelial cells, contributing to extracellular matrix (ECM) deposition and blood-brain barrier (BBB) formation, in addition to providing vasoactivity and stability (Bahrami and Childs, 2020; Daneman et al., 2010; Dave et al., 2018; Stratman et al., 2009). In animal models, an absence of brain pericytes results in hemorrhages and accelerates vascular-mediated neurodegeneration (Bell et al., 2010; Wang et al., 2014). Foxf2 is clearly important for vascular stability across species, as loss of Foxf2 in mice and zebrafish leads to increased brain hemorrhage and alterations in brain pericyte numbers and differentiation (Chauhan et al., 2016; Reyahi et al., 2015; Ryu et al., 2022). Brain tissue from patients with aging-related dementias (i.e. post-stroke dementia, vascular dementia, Alzheimer's disease) has reduced deep white matter pericytes and associated BBB disruption (Ding et al., 2020) suggesting that pericytes should be examined as mediators of CSVD progression in patients with FOXF2 deficiency.

We previously showed that complete loss of *foxf2* in *foxf2a*^{ca71}; *foxf2b*^{ca21} double-homozygous mutants in late embryogenesis leads to reduced brain pericyte numbers (Ryu et al., 2022). However, stroke susceptibility in humans is associated with reduced, but not absent,

FOXF2 expression. Genome-wide association (GWA) indicates that carrying a minor allele of an SNP in a *FOXF2* enhancer leads to reduced, but not absent, FOXF2 and is associated with stroke (Ryu et al., 2022). For this reason, we model CSVD using a zebrafish with reduced Foxf2 dosage using single homozygous *foxf2a* mutants. Zebrafish *foxf2a* and *foxf2b* genes are the result of genome duplication in zebrafish ~430 million years ago, and have similar gene expression (Arnold et al., 2015; Chauhan et al., 2016). We have detected no difference in function between the two genes, and therefore *foxf2a* loss of function may be similar to human heterozygous loss of FOXF2 function, a state that is observed in the population in GnomAD (Chen et al., 2024).

Strikingly, while pericytes in embryonic *foxf2* mutants are clearly affected, *foxf2* mutants can survive until adulthood, albeit with a reduced lifespan. How pericytes change across the lifespan while CSVD progresses is unknown.Here we find that *foxf2a* mutants have significantly reduced brain pericyte numbers as embryos that do not recover over time. Pericytes in mutant embryos and larvae exhibit morphological abnormalities, including increased soma size, longer processes, and degeneration. We show that processes and soma in the adults are also abnormal, though their morphology differs over the lifespan. Although the initial pool of pericytes is smaller, mutants can regenerate pericytes after ablation. Our analysis suggests that *foxf2* is required within pericytes to modulate numbers but also has a strong effect on morphology. We show that brain pericytes may contribute to the pathological progression of genetic CSVD, starting in embryonic development and continuing across the lifespan. Understanding the early developmental aspects of late-onset vascular conditions like CSVD will aid in the development of effective therapeutic strategies.

Results

Pericyte number is consistently lower in foxf2 mutant embryos and larvae

Embryonic phenotypes can lead to lifelong consequences. We have previously studied *foxf2a;foxf2b* double mutants only at a single embryonic stage at 3 days post fertilization (dpf). To understand how a pericyte and cerebrovascular phenotype evolves and/or resolves over development, we conducted serial imaging of individual brains of *foxf2a* mutants at embryonic stages (3 and 5 dpf), and at larval stages (7 and 10 dpf). Mutants were live imaged using endothelial *(kdrl:mCherry)* and pericyte *(pdgfrβ:Gal4, UAS:GFP)* transgenic lines.

Embryonically, brain pericytes have a thin-strand morphology and are closely associated with, and extend processes over, the endothelium in the midbrain and hindbrain of zebrafish (Fig. 1A-A''). In wildtype embryos, the number of pericytes increases progressively from 3

through 10 dpf (Fig. 1B). However, *foxf2a* mutants show significantly fewer pericytes on brain vessels at 3 dpf (Fig. 1C; mean 21 in wildtype and 10 in mutants) and this pericyte deficiency persists through 5, 7, and 10 dpf (Fig. 1C-D). The reduction in pericyte numbers shows variable penetrance, with some *foxf2a* mutants having pericyte numbers only slightly reduced from wildtype, and others that are severely diminished. The same pattern of pericyte reduction is seen with *foxf2a* mutants from a homozygous or heterozygous incross, suggesting there is no maternal effect (Fig. 1E-F). Serial imaging of mutants with regional absence in earlier stages shows that defects in pericyte coverage persist into later stages, suggesting that the size of the initial pericyte population is a key determinant of later coverage (Fig. S1). Double *foxf2a;foxf2b* mutants have a fully penetrant phenotype with significantly fewer brain pericytes in mutants than wildtype at every stage (Fig. S2; mean 19 in the wildtype and 9 in mutants at 3 dpf). Incomplete penetrance in *foxf2a* single mutants could be due to genetic compensation from *foxf2b*. While *foxf2b* is not significantly upregulated in *foxf2a* mutants on average, individual embryos have highly variable *foxf2b* expression (Fig. S3).

Since *Foxf2* conditional knockout mice show reduced expression of the pericyte marker *Pdgfrβ*, we tested whether *pdgfrβ* expression is *reduced* in *foxf*2a mutants, as this might introduce inaccuracies in pericyte counting. We used two methods, quantitative hybridization chain reaction (HCR) *in situ* hybridization and integrated density of the *pdgfrβ* transgene expression in wildtypes and mutants carrying only a single copy of the transgene. We show that *pdgfrβ* mRNA nor transgene expression is not reduced in *foxf2a* mutants (Fig. S3). Further, we show that *pdgfrβ* has complete overlap in expression with other brain pericyte markers such as *ndufa4l2* and *foxf2b* using HCR (Fig. 2A-D). Thus, *pdgfrβ* transgene or mRNA expression can reliably be used to count zebrafish brain pericytes in *foxf2a* mutants.

Although we focus on mural cells, Foxf2 is expressed in adult mouse brain endothelium (Vanlandewijck et al., 2018). We assessed *foxf2a* and *foxf2b* mRNA expression patterns using HCR *in situ* hybridization. At 3 dpf, *foxf2a* is co-localized with the pericyte marker *ndufa4l2a* in brain pericytes and shows low level co-localized expression with the blood vessel marker *kdrl* in brain endothelium (Fig. 2A). The expression pattern of *foxf2b* is similar. It is expressed in pericytes (*pdgfrβ*) and only weakly in endothelial cells (*kdrl*) (Fig 2B). This is supported by the DanioCell atlas of single-cell sequencing of multiple embryonic stages that shows expression of both genes is strongest in mural cells, pericytes and vascular smooth muscle cells and low in endothelial cells (Sur et al., 2023) (Fig. S4). Thus, while *foxf2a* and *foxf2b* are principally expressed in pericytes they are lowly expressed in endothelium during brain development.

Pericyte loss or impairment leads to alterations in vascular patterning in the mouse retina (Eilken et al., 2017). To assess if the endothelial network is affected in *foxf2a* mutants, we employed a Python workflow using Vessel Metrics (McGarry et al., 2024) (Fig. 2E). We found no statistical difference in total network length between wildtype and mutants at 3 dpf (Fig. 2F) or hindbrain central artery diameter (Fig. 2G). However, pericyte density (number of pericytes divided by the total network length) is reduced by 40% in *foxf2a* mutants (Fig. 2H), reflecting the loss of pericytes with no change in vessel network length. Similarly, pericyte coverage of vessels (total process coverage from brain pericytes divided by the total network length) is reduced by 39% in mutants (Fig. 2I). Our data suggest that during early development, *foxf2a* depletion primarily affects pericytes.

Early defects in brain vessel development have lifelong consequences.

foxf2 mutant animals can survive to adulthood, albeit with a reduced lifespan (~1 year vs. >2 years). Are early pericyte deficiencies repaired, or is loss of pericytes unimportant to survival to adulthood? To understand how brain pericyte phenotypes evolve over the lifespan, we dissected adult wildtype and *foxf2a* mutant brains on pericyte and endothelial double transgenic backgrounds and imaged after iDISCO clearing. Gross measurements of standard length of the fish (snout to tail) show no significant differences between wildtype and mutants, except that female mutant brain length and width are significantly smaller at 11 months post fertilization (mpf) (Fig. S5). However, there is no significant difference in the proportional brain length/standard length ratio in *foxf2a* mutants vs. wildtype.

Projected 3D views of light sheet images of the whole brain show striking defects in pericyte density, coverage and vascular pattern in *foxf2a* mutants vs. wildtype adults (Movie 1-2; Fig. 3A-B). Pericyte distribution is irregular, and blood vessel density is visibly reduced in mutant brains (Fig. 3C-D). Using a machine learning workflow (Fig. S6), we segmented pericyte soma, or the vessel backbone for the entire adult brain to count the total pericyte number in comparison to the total endothelial network length. We find a significant reduction in pericyte numbers in 3 mpf *foxf2a* mutant brains, which have only 45% of the pericytes of a wildtype brain (average of 24567 pericytes/brain vs. wildtype 54833 pericytes/brain; n=3 of each genotype; Fig. 3E). However, at this stage, the vessel network length is not statistically different (Fig. 3F). The density of pericytes on vessels is significantly decreased from 0.01 pericyte/μm to 0.006 pericytes/μm in *foxf2a* mutants showing a clear deficit (Fig. 3G). In contrast, the mean vessel diameter across vessel segments is not significantly different at 3 mpf when all diameters are

considered, nor when vessel diameters are grouped in 5 μm bins (n=522037 wildtype and 381544 *foxf2a* mutant diameters; Fig. 3H-I).

Similarly, cleared dissected brains at 11 mpf were imaged and show similarly striking vascular defects (Fig. S7). Adult pericytes have a clear, oblong cell body with long, slender primary processes that extend from the cytoplasm, and secondary processes that wrap around the circumference of the blood vessel (Fig. 3J). These pericytes form a continuous network of processes to cover the blood vessels in the brain. In *foxf2a* 11 mpf brains, pericyte somas lose their oblong shape, and cell bodies cannot be easily distinguished from processes. Mutant cells also extend thickened linear processes, with no secondary processes encircling the vessels. Mutant pericytes do not form an extensive network with other neighbouring pericytes. We note that there is variable phenotypic penetrance in *foxf2a* adults at 3 mpf that is reflective of the incomplete penetrance in *foxf2a* embryos (Fig. S7).

To view cellular morphology, we sectioned adult brains and immunolabeled pericytes and endothelium. In wildtype adult brains, we identified three subtypes of pericytes, ensheathing, mesh and thin-strand, previously characterized in murine models (Berthiaume et al., 2018a) (Fig. S8). In comparing brain sections from both wildtype and *foxf2a* mutants, on smaller vessels, mutant pericytes exhibit more linear processes with barely distinguishable soma, markedly differing from the characteristic appearance of wildtype adult pericytes (Fig. S9). Similarly, *pdgfrβ*-expressing cells on large-calibre vessels (mural cells, likely vascular Smooth Muscle cells (vSMCs)) show alterations in morphology and coverage (Fig. S9). Although mutant embryos do not exhibit apparent abnormalities in their endothelium, large aneurysm-like structures are evident in the adult brain (Fig. S10). These structures also appear to have decreased *kdrl* expression. Thus, both whole-mount and sectioned tissue show that brain vascular mural cell number and morphology are severely impacted in adult *foxf2a*$^{-/-}$ mutant brains, with increasing involvement of the endothelium, suggesting a worsening phenotype throughout life.

As *foxf2a* is expressed in vSMCs, we tested the effect of loss of *foxf2a* on vSMCs using confocal imaging of larvae and light sheet microscopy of cleared dissected 6 mpf adult wildtype and *foxf2a* mutant brains stained for transgenic endothelial (*kdrl*) and vSMC (*acta2*) markers. *acta2*-positive vSMCs are present on brain vessels around the Circle of Willis at embryonic (5 dpf) and larval (10 dpf) stages in both mutant and wildtype (Fig. 4A,C). Further, the number of vSMCs does not differ between mutant and wildtype (Fig. 4B,D). In adult brains, we find no significant difference in the total length of vSMCs in the brain, or in vSMC coverage (proportion

of vessels covered by vSMCs) (n=3 of each genotype; Movie 3-4; Fig. 4E-H). We note that at 6 mpf, there is a significant decrease in vessel network length however (Fig. 4G).

Morphological abnormalities emerge in the larval brain of mutants.

Considering the altered pericyte morphology of adult mutants, we revisited developmental stages to identify when these abnormalities first arise. We analyzed morphology at 3 and 10 dpf using in vivo confocal imaging to understand defects in the cell body (soma) and processes (Fig. 5A). We find no significant difference in the soma area at 3 dpf, but at 10 dpf, there is a significant increase in mutant pericyte soma area compared to wildtype (Fig. 5B). In parallel, wildtype pericytes undergo a slight reduction in soma size from 3 to 10 dpf.

The low number of brain pericytes in *foxf2a* mutants means that distinct pericyte processes can be distinguished and measured. However, in wildtypes, pericyte processes are not easily distinguished. For accurate process length measurements in wildtype we used multispectral labelling with a pericyte-specific Zebrabow transgenic line *(pdgfrβ:Gal4, UAS:Zebrabow)* (Pan et al., 2013; Whitesell et al., 2019). Cre mRNA was injected at the one-cell stage to activate random recombination, allowing us to visualize individual neighbouring pericytes (Fig. 5C). Wildtype processes have a mean length of 81.3 μm vs 102.9 in the mutant at 3 dpf and 96.3 μm vs 147.6 in the mutant at 10 dpf (Fig. 5D). Thus, the pericyte process lengths are significantly increased in *foxf2a* mutants at 3 and 10 dpf (Fig. 5D).

Through study of wildtype processes using multispectral labelling, we observed some differences in the behaviour of adjacent pericyte processes from that published in the adult mouse brain (Berthiaume et al., 2018b). While direct contact with no overlap between pericytes is the most common interaction in developing zebrafish, similar to mouse adult brain pericytes (Fig. 5F), we also see some overlap (Fig 5E). The average overlap between wildtype pericyte processes at 10 dpf was 5.9 μm (Fig. 5G). Together, our data show overlap in brain pericyte processes in wildtype animals.

To further explore mutant pericyte behaviour, we conducted serial imaging during larval development. Over time, some mutant pericyte processes form disconnected bead-like blebs with cell bodies that disappear over time (Fig. 6A). This pericyte phenotype can occur on vessels with full patency and is not associated with endothelial regression. The bead-like remnants are highly prevalent during larval development in *foxf2a*$^{-/-}$ mutants but not present in wildtype (Fig. 6B). To visualize process degeneration in real-time, we time-lapse imaged from 4-5 dpf (Fig. 6C). The pericyte can undergo a process reminiscent of cell death with soma

blebbing and process degeneration phenotypically resembling neural dendrite degeneration or pruning (Fig. 6D).

In summary, larval *foxf2a* mutant pericytes show reduced numbers, increased soma size, and elongated processes with evidence of process degeneration. In addition, we make the novel observation of overlapping pericyte processes during zebrafish development.

Foxf2a mutants do not have an impaired capacity to repopulate brain pericytes.

Zebrafish have regenerative capacity in various tissues (Becker et al., 1997; Lepilina et al., 2006; Otteson and Hitchcock, 2003), yet *foxf2a* mutant embryos that are pericyte-deficient maintain strong brain pericyte defects through aging which suggests that either they may not be able to replenish absent/damaged pericytes, or that the smaller size of the initial pool in embryogenesis limits repair such that numbers never can catch up to wildtype. To differentiate these hypotheses, we tested whether *foxf2a* mutants lack the capacity to regenerate pericytes. We reduced pericyte numbers in a *foxf2a* heterozygous incross using a cell ablation strategy. Zebrafish expressing *pdgfrβ:Gal4, UAS:NTR-mCherry* and *flk:GFP* transgenes were treated with 5 mM metronidazole (MTZ) at 50 hpf for 1 hour which ablates most pericytes. MTZ is a prodrug substrate that elicits cell death in nitroreductase (NTR)-expressing cells due to its cytotoxic derivatives. We then imaged and counted brain pericytes at 3 dpf (a day after treatment) and 10 dpf (recovery).

At 3 dpf, in the vehicle (DMSO) control group there is the expected significant difference between wildtype and mutant pericyte numbers (Fig. 7A-B). When treated with metronidazole, both mutants and wildtypes both have a similar, severe reduction in pericytes at 3 dpf post-ablation, and are not significantly different from each other (Fig. 7B). By 10 dpf, pericytes are partially repopulated in both wildtype and mutant ablated groups (Fig. 7C). Surprisingly, given the initial pericyte number defects in *foxf2a* mutant embryos, we find no significant difference between any groups (Fig. 7D; mean 70 in wildtype DMSO treated, 53 in mutant DMSO treated, 43 in wildtype MTZ treated, 33 in mutant MTZ treated). This shows that *foxf2a* mutants retain their ability to repopulate pericytes following ablation. This data is important to distinguish the timing and mechanism of pericyte reduction in *foxf2a* mutants. While *foxf2a* mutant pericytes can regenerate following induced catastrophic loss, it cannot compensate for the initially smaller pool of pericytes during embryogenesis. This data suggests that foxf2a plays a critical role in the establishment of a properly sized initial pericyte pool during early development. Regeneration mechanisms, although intact, cannot fully compensate for this initial reduction in pericytes.

Discussion

Our reduced dosage model of Foxf2 demonstrates disease processes at the cellular level in intact animals, giving insight into pathological changes that occur during CSVD that have not been observed in other models or humans. Our data supports a developmental origin for this type of CSVD, which then progresses and evolves across the lifespan (Fig. 8).

Dosage sensitivity of Foxf2

The logic for using a reduced dosage of Foxf2 in our studies is to better match the effect of common population variants leading to CSVD. We previously modelled the effect of a high-risk CSVD and stroke-associated SNV on the expression of FOXF2 in human cells, showing that it can reduce expression by ~50% (Ryu et al., 2022). Since zebrafish have two FOXF2 orthologs (foxf2a and foxf2b), foxf2a homozygotes have equivalent FOXF2 dosage as human heterozygotes, assuming that foxf2a and foxf2b not only exhibit similar expression but also share similar functions. Foxf2 is a dosage sensitive gene as zebrafish *foxf2a* hets show a significant reduction in brain pericytes. Similarly, mouse Foxf2 is also dosage sensitive (Reyahi et al., 2015). We find that *foxf2a* mutants are variably penetrant, while *foxf2a;foxf2b* double mutants are fully penetrant. Genetic compensation is common with gene duplication (Kok et al., 2015; Rouf et al., 2023) and would explain variability in disease phenotypes in different individuals with the same mutation.

Impaired embryonic pericyte coverage in Foxf2 deficiency

We show that numbers of brain pericytes are reduced at multiple developmental and adult stages when *foxf2a* and/or *foxf2a;foxf2b* are lost. The deficiency is significant at every stage, including 3 dpf, the earliest time point that pericytes are robustly observed in development. Deficient numbers could be due to a reduction in the pericyte precursor population (i.e. *nkx3.1* positive cells (Ahuja et al., 2024)), or to an inability of *foxf2a*-deficient cells to differentiate into *pdgfrβ*-positive pericytes. Our data does not allow us to distinguish these, although *pdgfrβ* expression in *foxf2a* mutants is transcriptionally unchanged, suggesting that pericyte number in early development is the primary phenotype. Additional evidence for pericytes being the primary cells affected is that there is no difference in total vessel network length or hindbrain CtA diameter at 3 dpf in *foxf2a* heterozygotes or mutants when pericyte numbers are reduced. A reduction in pericytes is expected to have early consequences, as pericytes provide signals to the endothelium for quiescence and arterial-venous identity (Mäe et al., 2021), as well as allowing contractility of cerebral blood vessels in early development (Bahrami and Childs, 2020). Fewer pericytes distributed on a normal-sized endothelial network length results in reduced

vessel coverage. It is intriguing therefore, that pericyte process length is increased at both 3 and 10 dpf, potentially to compensate for low pericyte density. A similar elongated pericyte phenotype and reduced coverage is seen in mice with constitutive *Pdgfβ*^{ret} knockout (Mäe et al., 2021). The convergent phenotypes after manipulation of two genes (*foxf2a* in fish and *Pdgfβ*^{ret} in mice) that reduce pericyte number suggest that the intrinsic pericyte response to depletion of pericyte density is to elongate, perhaps to attempt to cover 'naked' vessels. We note that previous mouse *Foxf2* knockouts using a conditional Wnt1-Cre driver saw contrasting results to ours, with increased pericyte numbers, although a similar loss of vascular stability is seen in both models (Reyahi et al., 2015). The reason for the difference in the direction in pericyte number may be experimental due to the different knockout technique (conditional in mice which only removes neural crest-derived pericytes vs. full knockout which removes mesodermal, neural crest-derived and endothelial *foxf2a* in fish) or the difference could reflect a species-specific difference.

Insights on fundamental pericyte process properties

The reasons behind the hypergrowth of pericyte processes in *foxf2a*$^{-/-}$ mutant brains is unclear. Berthiaume et al (2018a) propose that repulsive interactions among pericytes in the adult brain establish boundaries between adjacent pericytes, preventing their processes from overlapping. In this case, one might hypothesize that *foxf2a* mutant pericytes, which are less dense along vessels, would lack feedback from adjacent pericytes, leading to uncontrolled growth.

In mice, adult brain pericytes form a non-overlapping network along capillaries, although their processes occasionally approach each other without overlapping (Berthiaume et al., 2018b; Hill et al., 2015). Overlap between pericyte processes have not been well studied the developing brain, but *pdgfrb*$^{+ve}$ cells in developing zebrafish fin also overlap (Leonard et al., 2022). Strikingly, using multispectral (Zebrabow) labelling, we find processes overlap in the developing zebrafish brain. Overlaps occur on capillary segments and at branch points. Previous studies in mice were conducted in the adult brain, and it is possible that overlapping processes in the developing brain are transient, zebrafish-specific, or were potentially overlooked in the mouse experiments.

We have also observed forked extensions at the tips of some pericyte projections at 10 dpf in wildtype embryos, where pericytes are not in contact. Whether these unique structures are

involved in attractive/repulsive signals between pericytes or help determine the direction and extent of process growth is unclear, but understanding the fundamental mechanisms governing pericyte-pericyte process interactions would yield valuable insights into development and disease, as well as into how pericyte depletion results in abnormally long processes.

Morphological abnormalities in pericyte soma in foxf2a mutants

A second morphological abnormality of *foxf2a* deficient pericytes is that their soma size is increased at 10 dpf, which may also be a compensatory change. Pathological changes in soma size have not been observed in brain pericytes. However, increased neuronal soma size is observed in Amyotrophic Lateral Sclerosis or Lhermitte-Duclos disease (Dukkipati et al., 2018; Kwon et al., 2001) and is linked to mTor signaling (Kwon et al., 2003). In neuronal populations, moderate soma swelling can be an adaptation for survival, while rapid, drastic swelling indicates imminent death (Rousseau et al., 1999). It is therefore not surprising that we observe degeneration of pre-existing pericytes in *foxf2a* mutant but not wildtype animals. This degeneration phenotypically resembles neuronal dendrite remodelling and pruning during development (Fukui et al., 2012; Greenwood et al., 2007). Further work to test whether pericytes share similar mechanisms of degeneration in response to stress or cellular damage may provide further insight into phenotypic progression.

Changes in foxf2a mutants across the lifespan

For the first time, we have examined how vascular phenotypes change in the adult brain using iDISCO clearing. We find that adult soma take on very unusual, ‘stiff’ shapes and become almost indistinguishable from processes. The adult processes are shorter and more linear than the embryonic processes. Hypertrophic embryonic pericytes either do not survive to adulthood or undergo morphological changes over time. Given the limited knowledge in this area, the underlying factors driving this shift in pericyte morphology are unclear. Actin is present near the plasma membrane of cells, where it provides structural and mechanical support, enabling motility and determining cell structure. Given the abnormal shapes of adult pericytes, alterations in actin may contribute to their irregular morphology.

In the adult *foxf2a* mutant brain, abnormal *pdgfrβ*-expressing cells are observed on large-calibre vessels and likely represent vSMCs. We observed large-calibre aneurysm-like vessels, suggesting that vSMCs may lose functionality over time, thereby increasing the vulnerability of underlying vessels to dilation and weakening. Loss of *acta2* and, subsequently, vSMCs, has

been associated with conditions such as thoracic aortic aneurysms and dissections (Guo et al., 2009). However, we found no significant change in either vSMC cell number in embryonic development or in network length of vSMCs in the adult brain suggesting that the primary phenotype in *foxf2a* mutants is in pericyte cells, and that any changes to vSMCs are likely secondary.

Similarly, brain vessel diameter and network length are not significantly altered in embryonic *foxf2* mutants, but in 6-month-old adults, the vessel network length is significantly decreased. Our data suggests that *foxf2* deficiency contributes to cumulative vascular defects. Adult endothelial defects may be secondary to pericyte defects, although *foxf2a* is expressed in both pericytes and endothelial cells, and both cell types may be affected autonomously.

The initial pericyte pool is critical for lifelong vascular health

To understand the mechanism by which foxf2a influences pericyte numbers, we needed to distinguish between its role in early development and later roles. Our lab recently demonstrated that pericyte precursors express *nkx3.1* and *foxf2a* before pericyte differentiation and prior to expression of canonical markers such as *pdgfrβ* (Ahuja et al., 2024). Here we show that the pericyte pool in *foxf2a* mutants is reduced at the earliest embryonic stage that it can be measured. Zebrafish are remarkably regenerative and able to repair cardiac, retinal, spinal cord and pancreatic damage among other tissues (Poss and Tanaka, 2024). We therefore anticipated that *foxf2a* mutants might be able to regenerate new pericytes to replace lost pericytes. This was tested using genetic ablation of pericytes. Ablation is very efficient in mutants and wildtype. Surprisingly, 7 days after ablation, *foxf2a* mutants show recovery of pericyte numbers. Thus, when placed under extreme stress, embryonic *foxf2a* mutants can regenerate pericytes; yet, under baseline conditions, *foxf2a* mutant pericytes do not replenish. This experiment is important to distinguish an underlying mechanism of the *foxf2a* pericyte phenotype. Our data suggests that the earliest and most important difference in *foxf2a* mutant pericytes is their low initial number. Even though some repair is possible, it is not enough to compensate. Reduced pericyte density is associated with elongated processes, enlarged soma, and degeneration in mutants, which are likely signs of cellular stress. Over a lifetime, the deficiency leads to progressive damage to the vascular network. Determining that there is a critical embryonic window for developing a robust pericyte precursor pool helps us focus on early interventions to mitigate these deficits before damage over the lifespan worsens. The necessity of Foxf2 during development for the establishment of proper brain vasculature was

also seen in a mouse Foxf2 knockout (Reyahi et al., 2015). Further research into the early role of foxf2a in establishing initial pericyte specification/differentiation, and the impact of early vascular defects on disease progression, will be crucial for developing strategies to prevent and treat cerebrovascular conditions.

Materials and Methods

Zebrafish Husbandry and Strains

All procedures were conducted in compliance with the Canadian Council on Animal Care, and ethics approval was granted by the University of Calgary Animal Care Committee (AC21-0169). Embryos were maintained in E3 medium (5mM NaCl, 0.17mM KCl, 0.33mM CaCl2, 0.33mM MgSO4, pH = 7.2) (Westerfield, 2007) at 28°C. Larvae up to 10 dpf were maintained in an incubator with a light cycle (14 hours light, 10 hours darkness), with daily water changes and feeding. As zebrafish sex is not determined until 28 dpf, sex is not considered in embryo and larval experiments. For adult experiments, results were compared by sex where sufficient n's were available. Results from the progeny of het in-crosses were blinded in that they were quantified before genotyping. All reagents and strains are listed in Table 1 (Key Resources Table). All experiments included wildtype as a comparison group, and developmental stages, n's, and genotypes are noted for each experiment (Table 2).

Genotyping

Adult fish were anesthetized in 0.4% Tricaine (Sigma) and placed on a cutting surface. A small portion of the tip of the fin was clipped using a razor blade, and the fish were returned to the system to recover. For developmental DNA isolation, whole embryos, or larvae (up to 10 dpf) were anesthetized in 0.4% Tricaine prior to sampling.

Genomic DNA (gDNA) was extracted using the HotSHOT DNA isolation protocol, adapted from Kosuta et al., 2018. To isolate gDNA, tissue or embryo was placed in 50 µL of Base Solution and incubated at 95°C for 30 minutes. 5 µL of Neutralization Solution was added to neutralize the reaction. Samples were spun down in a mini centrifuge, and DNA was sampled from the top portion of the solution to avoid undigested samples.

Zebrafish were genotyped for target genes or the presence of transgenes using the KAPA2G Fast HotStart Genotyping Mix as per the manufacturer's instructions. *foxf2* mutants were genotyped using *foxf2a* primers (Table 1). A custom TaqMan probe for *foxf2b*^{ca22} (ANAACEC) was obtained from Applied Biosystems. Samples were genotyped using the QuantStudio 6 Flex Real-Time PCR System (Applied Biosystems) with the wildtype allele reported in FAM and the mutant allele reported in VIC.

In Situ Hybridization

Custom probes for *foxf2a* (PRD069), *nduf4al2* (RTD146), *kdrl* (PRI089), *pdgfrβ* (PRA654), and *foxf2b* (PRF462) were obtained from Molecular Instruments (Los Angeles, CA) for Hybridization Chain Reaction (HCR) in situ hybridization. In-situ staining was performed according to the manufacturer's instructions. Samples were permeabilized with proteinase K (1 mg/mL stock; Invitrogen, 4333793) at various times and concentrations, depending on their age.

Integrated Intensity

pdgfrβ and *foxf2b* intensity was obtained using ImageJ from in-situ stained embryos at 3dpf. Mean fluorescent intensity was measured using the freehand selection tool to circle each pericyte. The background mean intensity was subtracted from the pericyte mean intensity to standardize each measurement, and the intensities of each fish were averaged. The same protocol was used to measure the intensity of the *pdgfrβ* transgene in 3dpf live embryos.

Total RNA extraction and cDNA synthesis

Total RNA was extracted using the Research RNA Clean & Concentrator-5 Kit (Zymo Research, R1015) with some modifications. 50 dechorionated embryos were collected at 48 hpf, and homogenized in TRIZOL (Ambion, 15596026) reagent with a syringe needle. Briefly, samples were centrifuged at 16,000 rpm for 2 minutes to remove pigment. After separating the solution from the precipitate, chloroform was added, and the mixture was centrifuged at 12,000 rpm for 15 minutes at 4°C. The aqueous layer containing nucleic acids was removed, and an equal volume of 95-100% ethanol was added, then mixed well. The rest of the protocol followed the manufacturer's instructions using the Zymo-spin IC column. After eluting RNA with RNase/DNase-free water, samples were quantified using a Nanodrop to evaluate RNA quality. For cDNA synthesis, qSCRIPT cDNA Supermix (QuantaBio, 95048-100) was used according to the manufacturer's instructions and stored at -20°C.

RT-qPCR

To assess relative gene expression, real-time quantitative PCR (RT-qPCR) was carried out using custom-designed primers. PowerUP SYBR Green Master Mix (Applied Biosystems, A25742) was utilized on a QuantStudio 6 Flex Real-Time PCR System (Applied Biosystems). Cycle conditions followed the protocol of a PowerUP SYBR Green standard reaction: 50°C for 2 minutes, 95°C for 2 minutes, and 40 cycles of 95°C for 15 seconds and 60°C for 60 seconds. To calculate the fold change in gene expression, mutants were compared to wildtype using ΔΔCT calculations (Livak and Schmittgen, 2001).

Brain Dissection

Zebrafish were first euthanized in Tricaine and mounted on a Sylgard gel plate with dissection pins to stabilize them. Scissors were used to sever the brain stem entirely at the base of the head, posterior to the hindbrain. The eyes were removed with forceps/micro-scissors, and the optic stalks were cut. An incision was then made at the posterior portion of the skull plate anteriorly. Forceps were used to pull back the skull plate and orbital bones. Any nerve connections were severed, and the brains were removed and immediately fixed in ice-cold 4% PFA overnight at 4°C.

Brain Tissue Clearing

Whole zebrafish brains were cleared by either CUBIC (Susaki et al., 2015), or a modified iDISCO+ (Renier et al., 2016) protocol. For CUBIC, samples were incubated in 1:1 ratio of Reagent 1 (25% Quadrol (Sigma, 122262), 25% Urea, and 15% TritonX-100):H2O overnight at 37°C. Next, brains were incubated in 100% Reagent 1 at 37°C until the tissue was transparent. Finally, brains were rinsed in PBS, mounted in 2% low melting point agarose and re-placed in 100% Reagent 1 at 37°C until the tissue was transparent.

For iDISCO, the samples were first dehydrated in methanol:H_2O dilution series for 30 minutes each, then chilled at 4°C. Next, samples were incubated overnight in a 1:3 ratio of dichloromethane (DCM; Sigma, 270997):methanol at room temperature. The following day, samples were washed in methanol and then chilled at 4°C before bleaching in fresh 5% H_2O_2 in methanol overnight at 4°C. Then, samples were rehydrated in methanol:H2O dilution series for 30 minutes each, then washed in PTx.2 (0.2% TritonX-100 in PBS) twice over two hours at room temperature. Next, samples were incubated in permeabilization solution (0.3 M glycine, 20% DMSO in 400 mL PTx.2) at 37°C for up to two days, after which the samples were rinsed in PBS twice over one hour. Samples were then washed three times over two hours in 0.5 mM SDS/PBS at 37°C for three days before being incubated in primary antibody (Table 1) in 0.5 mM SDS/PBS at 37°C for two more days. The primary antibodies were refreshed in PTx.2 and left for another 4 days before overnight washing in PTwH (10 µg/ml heparin and 0.2% Tween-20 in PBS) at 37°C. Samples were left in secondary antibodies (Table 1) in PTwH/3% NSS at 37°C for 3 days, refreshed and left for another 3 days before washing overnight in PTwH. After immunolabeling, brains were mounted in 2% low melting agarose (LMA) and dehydrated in methanol:H_2O dilution series for 30 minutes each and left overnight at room temperature. Next, brains were incubated in a 1:3 ratio of DCM: methanol at room temperature for three hours

before washing in 100% DCM for 15 minutes twice. Finally, brains were incubated in Ethyl cinnamate (Sigma, NSC6773) for two hours before replacing the solution and incubating overnight at room temperature.

Tissue Sectioning

For vibratome sections, brains were fixed in 4% PFA, washed and mounted in 4% LMA (Invitrogen, 16520-050) before sectioning with a vibratome (Leica, VT1000S) to obtain a series of transverse sections at 50 µm.

Cre mRNA Injections

Wildtype fish on a Zebrabow transgenic background (Pan et al., 2013) were injected with 1pg of Cre mRNA at the one-cell stage. Embryos were kept in E3 at 28°C until imaging.

Immunofluorescence

Sections for immunofluorescence were briefly washed in PBS, followed by 2% TritonX-100 in PBS for permeabilization. Sections were moved from the permeabilization solution into blocking buffer (5% Goat serum, 3% BSA, 0.2% TritonX-100 in PBS) for 1 hour before incubation in primary antibody. Sections were then washed and left in secondary antibodies for 3 hours at room temperature. After incubation, sections were washed, mounted and cover slipped with Fluoromount-G™ Mounting Medium, with DAPI or without counterstain.

Drug Treatments

Embryos were dechorionated prior to treatment, and all drug treatments included DMSO at an equivalent concentration to the drug solution as a control (Sigma, D8418). Treatments were performed in a 24-well plate with approximately 15 embryos per well. For pericyte ablation experiments, 5 mM Metronidazole (MTZ; Sigma, M3761) was applied at 50 hpf for 1 hour with a DMSO control.

Microscopy

Imaging fluorescent transgene expression in live embryos, antibody staining, and fluorescent staining were completed using an inverted laser scanning confocal microscope (LSM900; Zeiss) with a 10X (0.25 NA), 20X (0.8 NA), 40X water (1.1 NA) or 60X (1.4 NA) oil objectives. Laser wavelengths included blue (405 nm), green (488 nm), red (561 nm), and far red (640 nm). Embryos were maintained in Phenylthiourea (PTU) from 24 hpf onwards to prevent pigment development, anesthetized in 0.4% tricaine and mounted in 0.8% LMA dissolved in E3, on a clear imaging dish. In some cases, live samples were retrieved from the agarose following

imaging for further imaging at later time points, genotyping, or other data collection. Images were processed using Zen Blue and Fiji (Schindelin et al., 2012) software.

Imaging of whole adult brains was completed using the Light-sheet microscope (Ultramicroscope II equipped with a SuperPlan module; Miltenyi Biotec) with a 4X (0.35 NA) objective at 1.0 zoom. Laser wavelengths included green (488 nm) and red (561 nm). Images were processed using Zen Blue, Fiji and Imaris software.

Vessel network quantitation

Confocal images from embryos were analyzed using the Python-based software tool Vessel Metrics (McGarry et al., 2024). The total vessel network length was measured starting from below the middle cerebral vein and dorsal longitudinal vein until the emergence of the basal communicating artery. Vessels included in measurements are as follows: middle mesencephalic central arteries, posterior mesencephalic central arteries, the primordial hindbrain channels and the posterior region of the basilar artery. The forebrain vessels (i.e. anterior cerebral veins) were not included. Blood vessel diameter was restricted to the horizontal hindbrain central arteries, which were comparable between all images.

Adult vessel network length was measured using Ilastik (Berg et al., 2019) and Imaris (version 10.2.0; Bitplane AG, Oxford Instruments) software. Vessels were annotated in Ilastik to obtain a probability map. The probability map was imported into Imaris as a new channel for each image. The surface tool with machine learning was then used to annotate the vessels a second time, using the Ilastik map as the training guide. A mask was created from this surface. The filament tool was then used to create a 3D network of the vessel, using the surface mask as a training guide. The total network length and the diameter of each vessel segment were exported from the filament statistics tab.

Smooth muscle cell coverage was measured using the same pipeline; however, the raw channel was used for the surface tool annotation without using Ilastik. Total network length was exported from the filament statistics tab.

Pericyte quantitation

Embryonic pericytes were manually counted using the Fiji counting or tracing tool on flattened Z-stacks from confocal images of the whole zebrafish head. Pericyte counting and analysis were restricted to the mid and hindbrain regions for all metrics. For pericyte process lengths,

individual processes extending from a single soma were measured and summed to determine the total process length per pericyte (μm). In instances where two processes appeared to merge or cover the same blood vessel, half of the total length was added to each pericyte. For Zebrabow images, only pericytes with processes distinguishable from neighbouring pericytes were measured. For soma size, individual cell bodies were traced, and the area was determined by the software in μm^2.

Adult pericytes were counted using the spot tool in Imaris. Using the raw channel, the spot tool was trained to identify pericyte cell bodies. The total spot number, equivalent to the number of pericyte cell bodies, was exported from the spot statistics tab. A mask of the spot tool was created to better visualize pericytes.

Statistics

All statistical analyses were performed using GraphPad Prism 10, with significance determined by $p < 0.05$. Statistical tests conducted are included in figure captions. If no significance is indicated, it is not significant. The D'Agostino-Pearson test was used to assess the normality of data sets, and in cases where the data did not pass the normality test, non-parametric statistics were used. Experimental N's are reported in Table 2. Results are expressed on graphs as mean ± standard deviation (SD). Only significant p-values are indicated.

Acknowledgements

This work was funded by the Canadian Institutes of Health Research PJT-183631. MFG received a Canada Graduate Scholarship Master's from Canadian Institutes of Health Research, the Alberta Graduate Excellence Scholarship (AGES) for Master's Research from the Province of Alberta, and a Biochemistry and Molecular Biology Department scholarship from the University of Calgary. EH received the Alvin Libin Graduate Scholarship in Cardiovascular Research, the Alberta Children's Hospital Research Institute (ACHRI) Graduate Scholarship for Master's Research, the ACHRI Graduate Scholarship for Doctoral Research, and the Alberta Graduate Excellence Scholarship (AGES) for Doctoral Research from the Province of Alberta. We acknowledge the Alberta Children's Hospital Research Institute and Hotchkiss Brain Institute Imaging facilities for microscopes and technical support.

References

Ahuja, S., Adjekukor, C., Li, Q., Kocha, K. M., Rosin, N., Labit, E., Sinha, S., Narang, A., Long, Q., Biernaskie, J., et al. (2024). The development of brain pericytes requires expression of the transcription factor nkx3.1 in intermediate precursors. *PLoS Biol.* **22**, e3002590.

Arnold, C. R., Lamont, R. E., Walker, J. T., Spice, P. J., Chan, C., Ho, C. and Childs, S. J. (2015). Comparative analysis of genes regulated by Dzip1/ *iguana* and hedgehog in zebrafish. *Dev. Dyn.* **244**, 211–223.

Bahrami, N. and Childs, S. J. (2020). Development of vascular regulation in the zebrafish embryo. *Dev. Camb. Engl.* **147**, dev183061.

Becker, T., Wullimann, M. F., Becker, C. G., Bernhardt, R. R. and Schachner, M. (1997). Axonal regrowth after spinal cord transection in adult zebrafish. *J. Comp. Neurol.* **377**, 577–595.

Bell, R. D., Winkler, E. A., Sagare, A. P., Singh, I., LaRue, B., Deane, R. and Zlokovic, B. V. (2010). Pericytes control key neurovascular functions and neuronal phenotype in the adult brain and during brain aging. *Neuron* **68**, 409–427.

Berg, S., Kutra, D., Kroeger, T., Straehle, C. N., Kausler, B. X., Haubold, C., Schiegg, M., Ales, J., Beier, T., Rudy, M., et al. (2019). ilastik: interactive machine learning for (bio)image analysis. *Nat. Methods* **16**, 1226–1232.

Berthiaume, A.-A., Hartmann, D. A., Majesky, M. W., Bhat, N. R. and Shih, A. Y. (2018a). Pericyte Structural Remodeling in Cerebrovascular Health and Homeostasis. *Front. Aging Neurosci.* **10**, 210.

Berthiaume, A.-A., Grant, R. I., McDowell, K. P., Underly, R. G., Hartmann, D. A., Levy, M., Bhat, N. R. and Shih, A. Y. (2018b). Dynamic Remodeling of Pericytes In Vivo Maintains Capillary Coverage in the Adult Mouse Brain. *Cell Rep.* **22**, 8–16.

Chauhan, G., Arnold, C. R., Chu, A. Y., Fornage, M., Reyahi, A., Bis, J. C., Havulinna, A. S., Sargurupremraj, M., Smith, A. V., Adams, H. H. H., et al. (2016). Identification of additional risk loci for stroke and small vessel disease: a meta-analysis of genome-wide association studies. *Lancet Neurol.* **15**, 695–707.

Chen, S., Francioli, L. C., Goodrich, J. K., Collins, R. L., Kanai, M., Wang, Q., Alföldi, J., Watts, N. A., Vittal, C., Gauthier, L. D., et al. (2024). A genomic mutational constraint map using variation in 76,156 human genomes. *Nature* **625**, 92–100.

Daneman, R., Zhou, L., Kebede, A. A. and Barres, B. A. (2010). Pericytes are required for blood-brain barrier integrity during embryogenesis. *Nature* **468**, 562–566.

Dave, J. M., Mirabella, T., Weatherbee, S. D. and Greif, D. M. (2018). Pericyte ALK5/TIMP3 Axis Contributes to Endothelial Morphogenesis in the Developing Brain. *Dev. Cell* **47**, 388–389.

Ding, R., Hase, Y., Ameen-Ali, K. E., Ndung'u, M., Stevenson, W., Barsby, J., Gourlay, R., Akinyemi, T., Akinyemi, R., Uemura, M. T., et al. (2020). Loss of capillary pericytes and the blood-brain barrier in white matter in poststroke and vascular dementias and Alzheimer's disease. *Brain Pathol. Zurich Switz.* **30**, 1087–1101.

Dukkipati, S. S., Garrett, T. L. and Elbasiouny, S. M. (2018). The vulnerability of spinal motoneurons and soma size plasticity in a mouse model of amyotrophic lateral sclerosis. *J. Physiol.* **596**, 1723–1745.

Duperron, M.-G., Knol, M. J., Le Grand, Q., Evans, T. E., Mishra, A., Tsuchida, A., Roshchupkin, G., Konuma, T., Trégouët, D.-A., Romero, J. R., et al. (2023). Genomics of perivascular space burden unravels early mechanisms of cerebral small vessel disease. *Nat. Med.* **29**, 950–962.

Eilken, H. M., Diéguez-Hurtado, R., Schmidt, I., Nakayama, M., Jeong, H.-W., Arf, H., Adams, S., Ferrara, N. and Adams, R. H. (2017). Pericytes regulate VEGF-induced endothelial sprouting through VEGFR1. *Nat. Commun.* **8**, 1574.

Fukui, K., Ushiki, K., Takatsu, H., Koike, T. and Urano, S. (2012). Tocotrienols prevent hydrogen peroxide-induced axon and dendrite degeneration in cerebellar granule cells. *Free Radic. Res.* **46**, 184–193.

Greenwood, S. M., Mizielinska, S. M., Frenguelli, B. G., Harvey, J. and Connolly, C. N. (2007). Mitochondrial dysfunction and dendritic beading during neuronal toxicity. *J. Biol. Chem.* **282**, 26235–26244.

Guo, D.-C., Papke, C. L., Tran-Fadulu, V., Regalado, E. S., Avidan, N., Johnson, R. J., Kim, D. H., Pannu, H., Willing, M. C., Sparks, E., et al. (2009). Mutations in smooth muscle alpha-actin (ACTA2) cause coronary artery disease, stroke, and Moyamoya disease, along with thoracic aortic disease. *Am. J. Hum. Genet.* **84**, 617–627.

Hill, R. A., Tong, L., Yuan, P., Murikinati, S., Gupta, S. and Grutzendler, J. (2015). Regional Blood Flow in the Normal and Ischemic Brain Is Controlled by Arteriolar Smooth Muscle Cell Contractility and Not by Capillary Pericytes. *Neuron* **87**, 95–110.

Kok, F. O., Shin, M., Ni, C.-W., Gupta, A., Grosse, A. S., van Impel, A., Kirchmaier, B. C., Peterson-Maduro, J., Kourkoulis, G., Male, I., et al. (2015). Reverse genetic screening reveals poor correlation between morpholino-induced and mutant phenotypes in zebrafish. *Dev. Cell* **32**, 97–108.

Kwon, C. H., Zhu, X., Zhang, J., Knoop, L. L., Tharp, R., Smeyne, R. J., Eberhart, C. G., Burger, P. C. and Baker, S. J. (2001). Pten regulates neuronal soma size: a mouse model of Lhermitte-Duclos disease. *Nat. Genet.* **29**, 404–411.

Kwon, C.-H., Zhu, X., Zhang, J. and Baker, S. J. (2003). mTor is required for hypertrophy of Pten-deficient neuronal soma in vivo. *Proc. Natl. Acad. Sci. U. S. A.* **100**, 12923–12928.

Leonard, E. V., Figueroa, R. J., Bussmann, J., Lawson, N. D., Amigo, J. D. and Siekmann, A. F. (2022). Regenerating vascular mural cells in zebrafish fin blood vessels are not derived from pre-existing mural cells and differentially require Pdgfrb signalling for their development. *Dev. Camb. Engl.* **149**, dev199640.

Lepilina, A., Coon, A. N., Kikuchi, K., Holdway, J. E., Roberts, R. W., Burns, C. G. and Poss, K. D. (2006). A dynamic epicardial injury response supports progenitor cell activity during zebrafish heart regeneration. *Cell* **127**, 607–619.

Livak, K. J. and Schmittgen, T. D. (2001). Analysis of relative gene expression data using real-time quantitative PCR and the 2(-Delta Delta C(T)) Method. *Methods San Diego Calif* **25**, 402–408.

Mäe, M. A., He, L., Nordling, S., Vazquez-Liebanas, E., Nahar, K., Jung, B., Li, X., Tan, B. C., Chin Foo, J., Cazenave-Gassiot, A., et al. (2021). Single-Cell Analysis of Blood-Brain Barrier Response to Pericyte Loss. *Circ. Res.* **128**, e46–e62.

McGarry, S. D., Adjekukor, C., Ahuja, S., Greysson-Wong, J., Vien, I., Rinker, K. D. and Childs, S. J. (2024). Vessel Metrics: A software tool for automated analysis of vascular structure in confocal imaging. *Microvasc. Res.* **151**, 104610.

Østergaard, L., Engedal, T. S., Moreton, F., Hansen, M. B., Wardlaw, J. M., Dalkara, T., Markus, H. S. and Muir, K. W. (2016). Cerebral small vessel disease: Capillary pathways to stroke and cognitive decline. *J. Cereb. Blood Flow Metab. Off. J. Int. Soc. Cereb. Blood Flow Metab.* **36**, 302–325.

Otteson, D. C. and Hitchcock, P. F. (2003). Stem cells in the teleost retina: persistent neurogenesis and injury-induced regeneration. *Vision Res.* **43**, 927–936.

Pan, Y. A., Freundlich, T., Weissman, T. A., Schoppik, D., Wang, X. C., Zimmerman, S., Ciruna, B., Sanes, J. R., Lichtman, J. W. and Schier, A. F. (2013). Zebrabow: multispectral cell labeling for cell tracing and lineage analysis in zebrafish. *Dev. Camb. Engl.* **140**, 2835–2846.

Poss, K. D. and Tanaka, E. M. (2024). Hallmarks of regeneration. *Cell Stem Cell* **31**, 1244–1261.

Renier, N., Adams, E. L., Kirst, C., Wu, Z., Azevedo, R., Kohl, J., Autry, A. E., Kadiri, L., Umadevi Venkataraju, K., Zhou, Y., et al. (2016). Mapping of Brain Activity by Automated Volume Analysis of Immediate Early Genes. *Cell* **165**, 1789–1802.

Reyahi, A., Nik, A. M., Ghiami, M., Gritli-Linde, A., Pontén, F., Johansson, B. R. and Carlsson, P. (2015). Foxf2 Is Required for Brain Pericyte Differentiation and Development and Maintenance of the Blood-Brain Barrier. *Dev. Cell* **34**, 19–32.

Rouf, M. A., Wen, L., Mahendra, Y., Wang, J., Zhang, K., Liang, S., Wang, Y., Li, Z., Wang, Y. and Wang, G. (2023). The recent advances and future perspectives of genetic compensation studies in the zebrafish model. *Genes Dis.* **10**, 468–479.

Rousseau, V., Engelmann, R. and Sabel, B. A. (1999). Restoration of vision III: soma swelling dynamics predicts neuronal death or survival after optic nerve crush in vivo. *Neuroreport* **10**, 3387–3391.

Ryu, J.-R., Ahuja, S., Arnold, C. R., Potts, K. G., Mishra, A., Yang, Q., Sargurupremraj, M., Mahoney, D. J., Seshadri, S., Debette, S., et al. (2022). Stroke-associated intergenic

variants modulate a human FOXF2 transcriptional enhancer. *Proc. Natl. Acad. Sci. U. S. A.* **119**, e2121333119.

Schindelin, J., Arganda-Carreras, I., Frise, E., Kaynig, V., Longair, M., Pietzsch, T., Preibisch, S., Rueden, C., Saalfeld, S., Schmid, B., et al. (2012). Fiji: an open-source platform for biological-image analysis. *Nat. Methods* **9**, 676–682.

Stratman, A. N., Malotte, K. M., Mahan, R. D., Davis, M. J. and Davis, G. E. (2009). Pericyte recruitment during vasculogenic tube assembly stimulates endothelial basement membrane matrix formation. *Blood* **114**, 5091–5101.

Sur, A., Wang, Y., Capar, P., Margolin, G. and Farrell, J. A. (2023). Single-cell analysis of shared signatures and transcriptional diversity during zebrafish development. *BioRxiv Prepr. Serv. Biol.* 2023.03.20.533545.

Susaki, E. A., Tainaka, K., Perrin, D., Yukinaga, H., Kuno, A. and Ueda, H. R. (2015). Advanced CUBIC protocols for whole-brain and whole-body clearing and imaging. *Nat. Protoc.* **10**, 1709–1727.

Vanlandewijck, M., He, L., Mäe, M. A., Andrae, J., Ando, K., Del Gaudio, F., Nahar, K., Lebouvier, T., Laviña, B., Gouveia, L., et al. (2018). A molecular atlas of cell types and zonation in the brain vasculature. *Nature* **554**, 475–480.

Wang, Y., Pan, L., Moens, C. B. and Appel, B. (2014). Notch3 establishes brain vascular integrity by regulating pericyte number. *Dev. Camb. Engl.* **141**, 307–317.

Westerfield, M. (2007). *THE ZEBRAFISH BOOK, 5th Edition; A guide for the laboratory use of zebrafish (Danio rerio)*. Eugene: University of Oregon Press.

Whitesell, T. R., Chrystal, P. W., Ryu, J.-R., Munsie, N., Grosse, A., French, C. R., Workentine, M. L., Li, R., Zhu, L. J., Waskiewicz, A., et al. (2019). foxc1 is required for embryonic head vascular smooth muscle differentiation in zebrafish. *Dev. Biol.* **453**, 34–47.

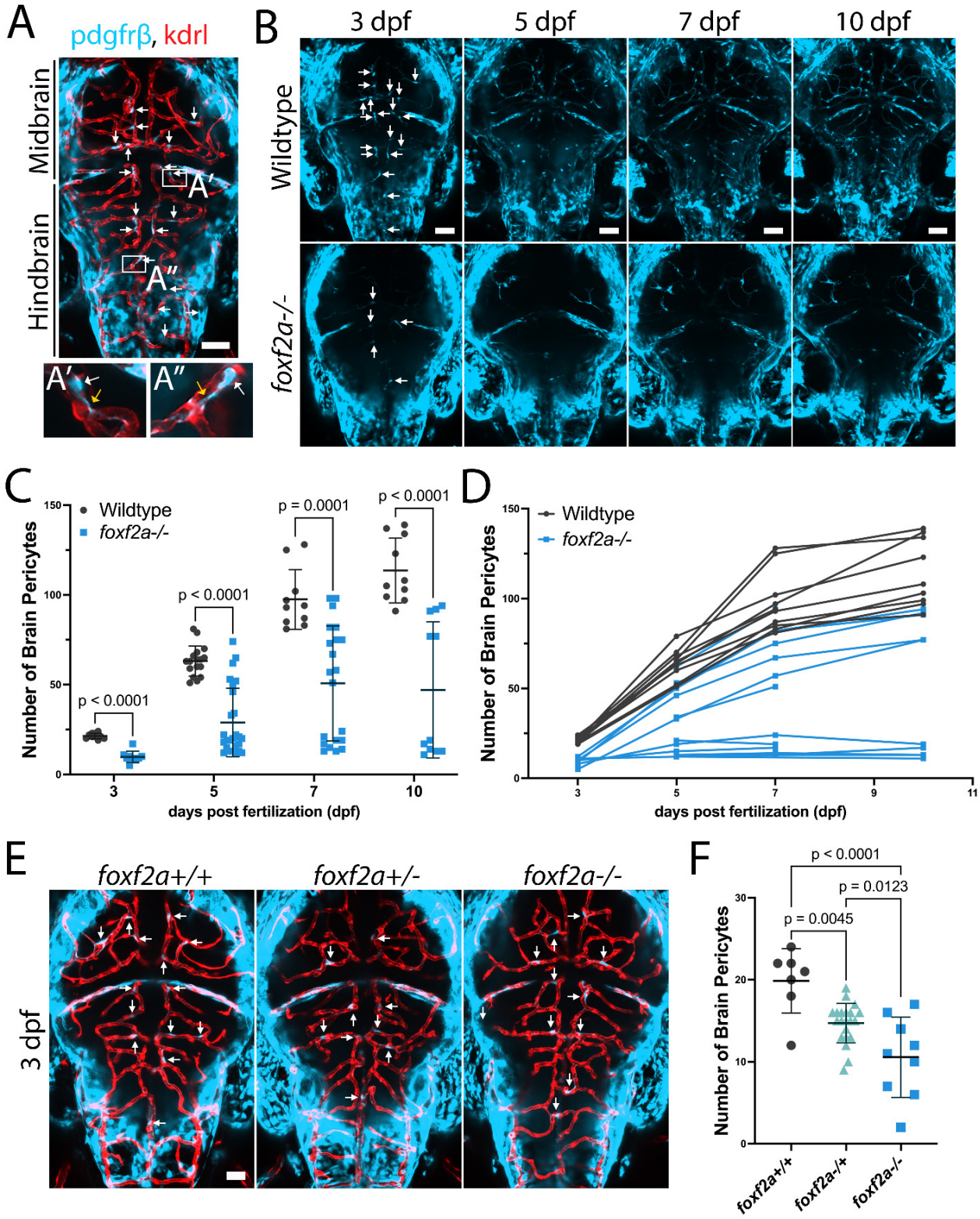

Figure 1. Brain pericyte number is consistently lower and does not recover in *foxf2a* mutant larvae. (A) Zebrafish brains were imaged using endothelial (red; *Tg(kdrl:mCherry)*) and pericyte (light blue; *Tg(pdgfrβ:Gal4, UAS:GFP)*) transgenic lines (arrows: brain pericytes). (A'-A'') Brain pericyte soma (white arrows) and processes (yellow arrows) are closely associated with the endothelium. (B) Serially imaged wildtype and *foxf2a* mutant brains at 3, 5, 7 and 10 dpf. (C) Total brain pericyte

numbers at 3, 5, 7 and 10 dpf. (D) Individual brain pericyte trajectories of serially imaged embryos over the same period. (E) Dorsal images of embryos for the indicated genotypes from a *foxf2a* heterozygous incross at 75 hpf. (F) Total brain pericytes at 75 hpf. Statistical analysis was conducted using multiple Mann-Whitney tests (C) and one-way ANOVA with Tukey's test (F). Scale bars, 50 μm (A-B, E).

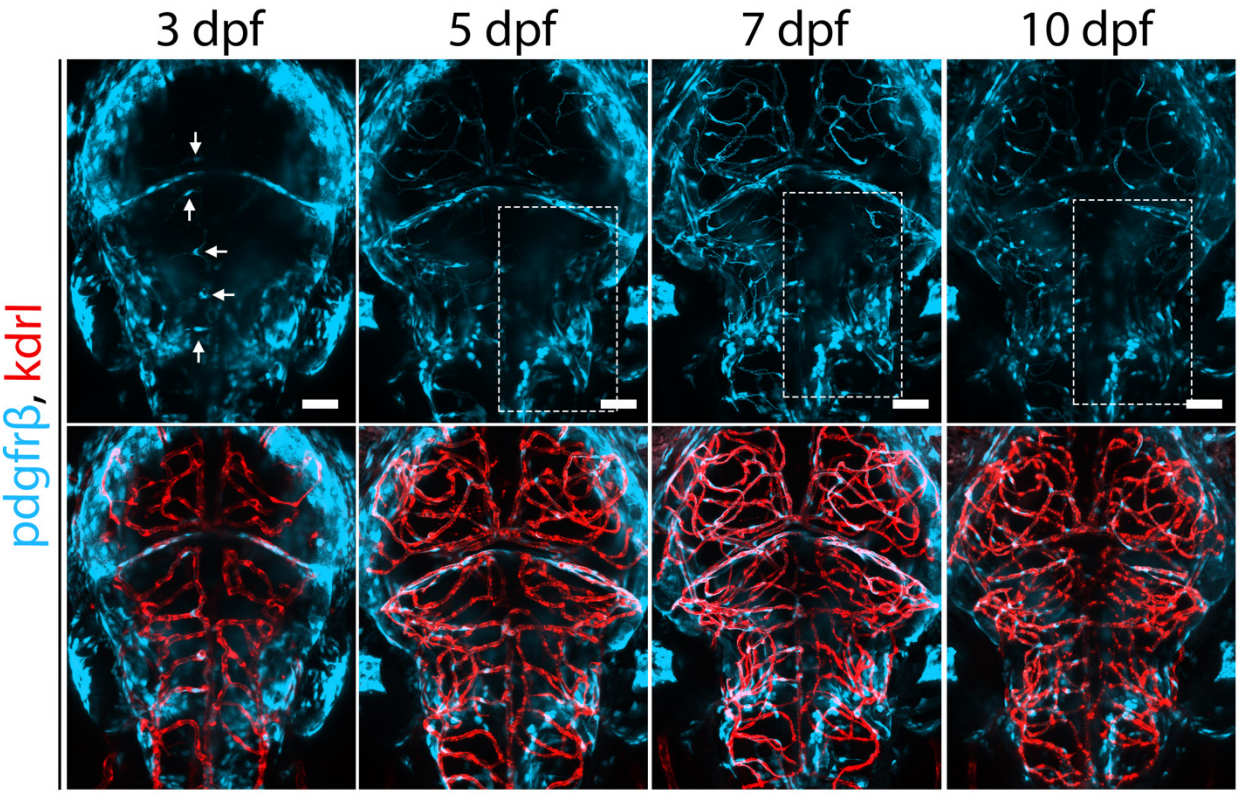

Supplemental Figure 1. *foxf2a* mutants exhibit regional loss. Serial imaging of a *foxf2a-/-* mutant brain at 3, 5, 7 and 10 dpf (arrows: brain pericytes; boxes: regional loss). Scale bars, 50 µm.

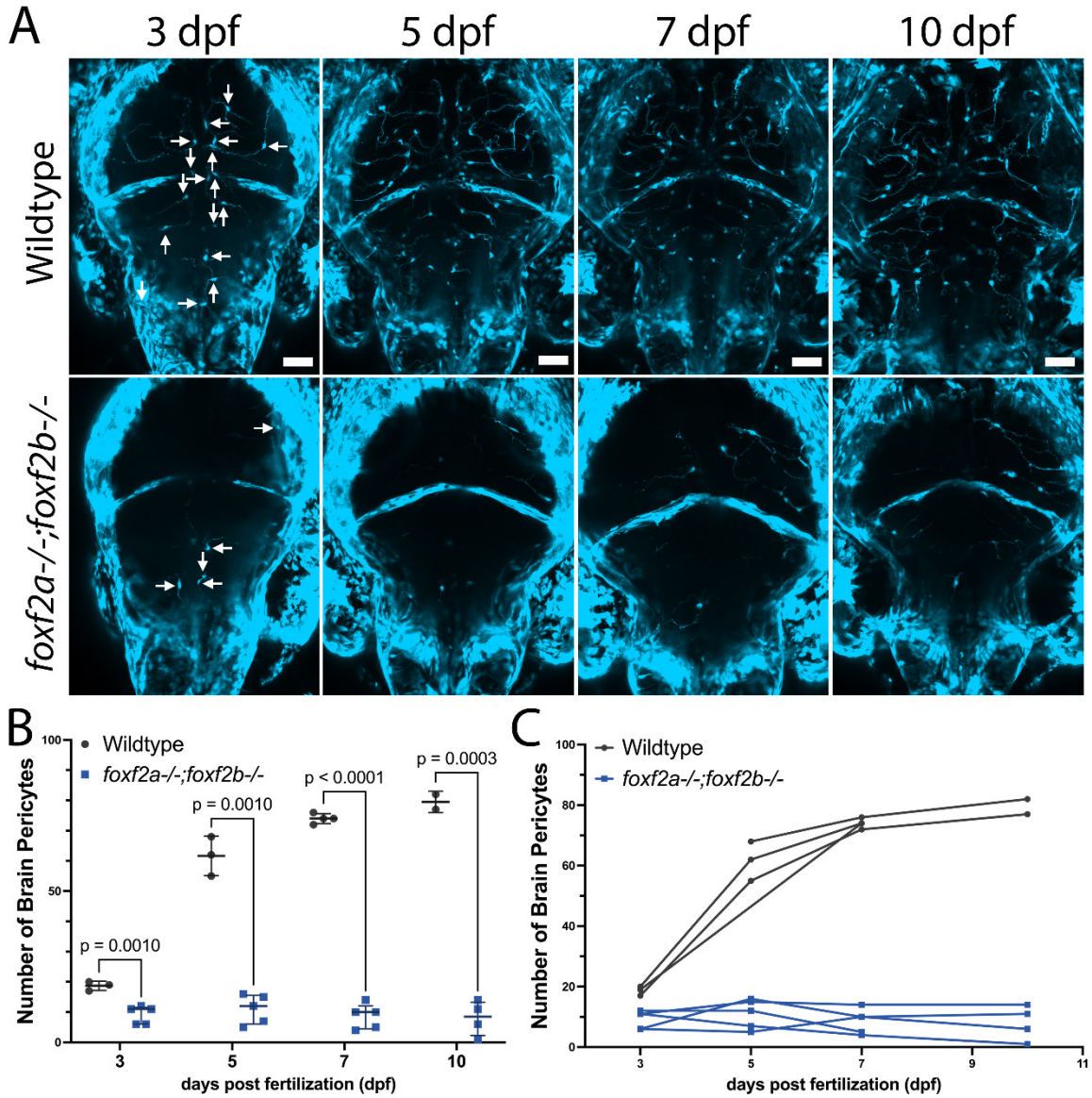

Supplemental Figure 2. foxf2 knockouts have severe pericyte deficiency during development. (A) Serial imaging of wildtype and *foxf2a-/-;foxf2b-/-* double mutant brains at 3, 5, 7 and 10 dpf (arrows: brain pericytes). (B) Scatter plot of total brain pericyte numbers at 3, 5, 7 and 10 dpf. (C) Individual mutant trajectories over the same period. Statistical analysis was conducted using multiple unpaired t-tests with Welch corrections. Scale bars, 50 μm (A).

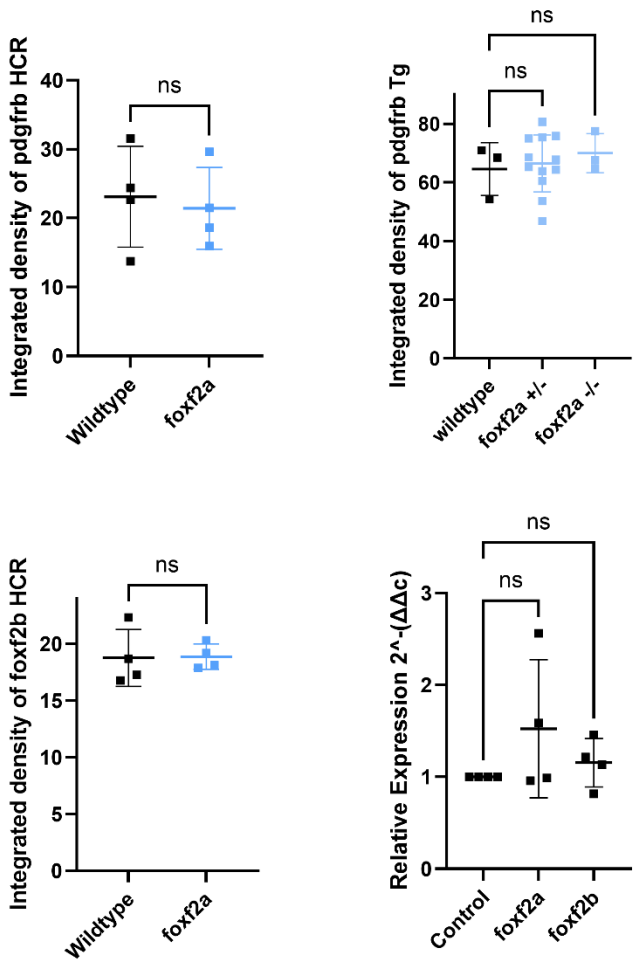

Supplemental Figure 3. *pdgfrβ* mRNA and transgene have similar expression in wildtype and *foxf2a* mutants. *foxf2b* expression is not upregulated in mutants. A) Integrated intensity of *pdgfrβ* expression by HCR. B) Integrated density of confocal imaged *pdgfrβ* transgene expression in wildtype, *foxf2a* heterozygote and *foxf2a* homozygote mutants. C) Integrated density of *foxf2b* expression in *foxf2a* mutants by HCR. D) Relative expression by qPCR of *foxf2a* and *foxf2b* expression in *foxf2a* mutants. Statistics in A, C use the Student's t-test while B and D use Anova with Bartlett's test. None of the comparisons are significant (ns).

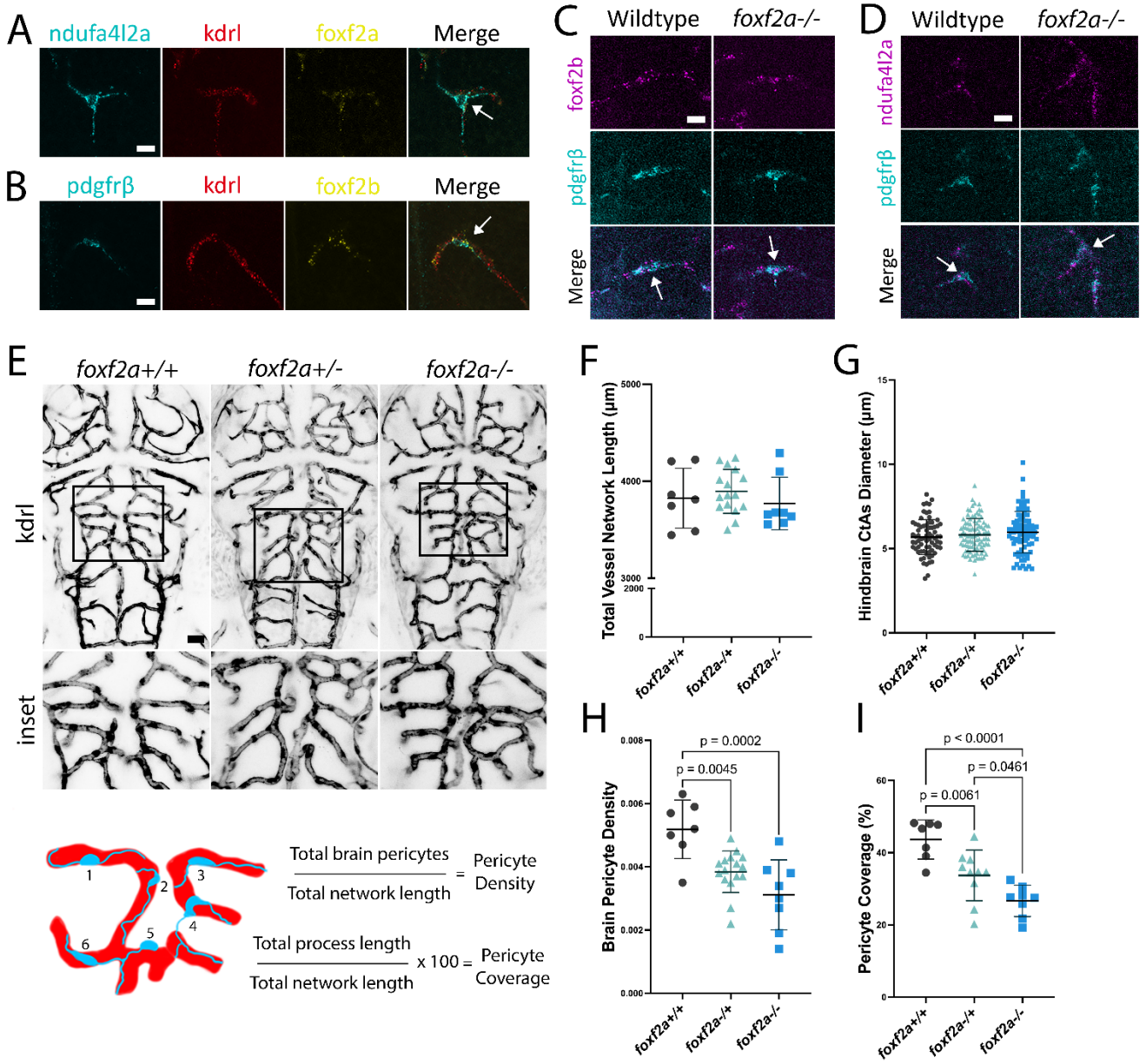

Figure 2. *Loss of foxf2* affects embryonic pericyte numbers, but not endothelial cell pattern. (A) *foxf2a* expression in wildtype brains at 72 hpf using Hybridization Chain Reaction (HCR) shows co-expression with pericyte marker *ndufa4l2a. foxf2a* is also lowly co-expressed in the endothelium with *kdrl*. Arrows show overlapping expression. (B) *foxf2b* is co-expressed with pericyte marker *pdgfrβ* also lowly expressed in the endothelium (*kdrl*). (C) *foxf2b* and *pdgfrβ* are expressed in a similar, overlapping pattern in pericytes of wildtype and *foxf2a* mutants. (D) Pericyte marker *nduf4al2a* and *pdgfrβ* are expressed in a similar, overlapping pattern in pericytes in wildtype and *foxf2a* mutants. (E) Image of endothelium used to generate the total blood vessel network length. (F) Total vessel network length from Vessel Metrics software. (G) Scatter plot of hindbrain CtA diameters. (H) Scatter plot of pericyte density and pericyte coverage (I). Statistical analysis was conducted using one-way ANOVA with Tukey's test. Scale bars, 10 µm (A-D), 50 µm (F).

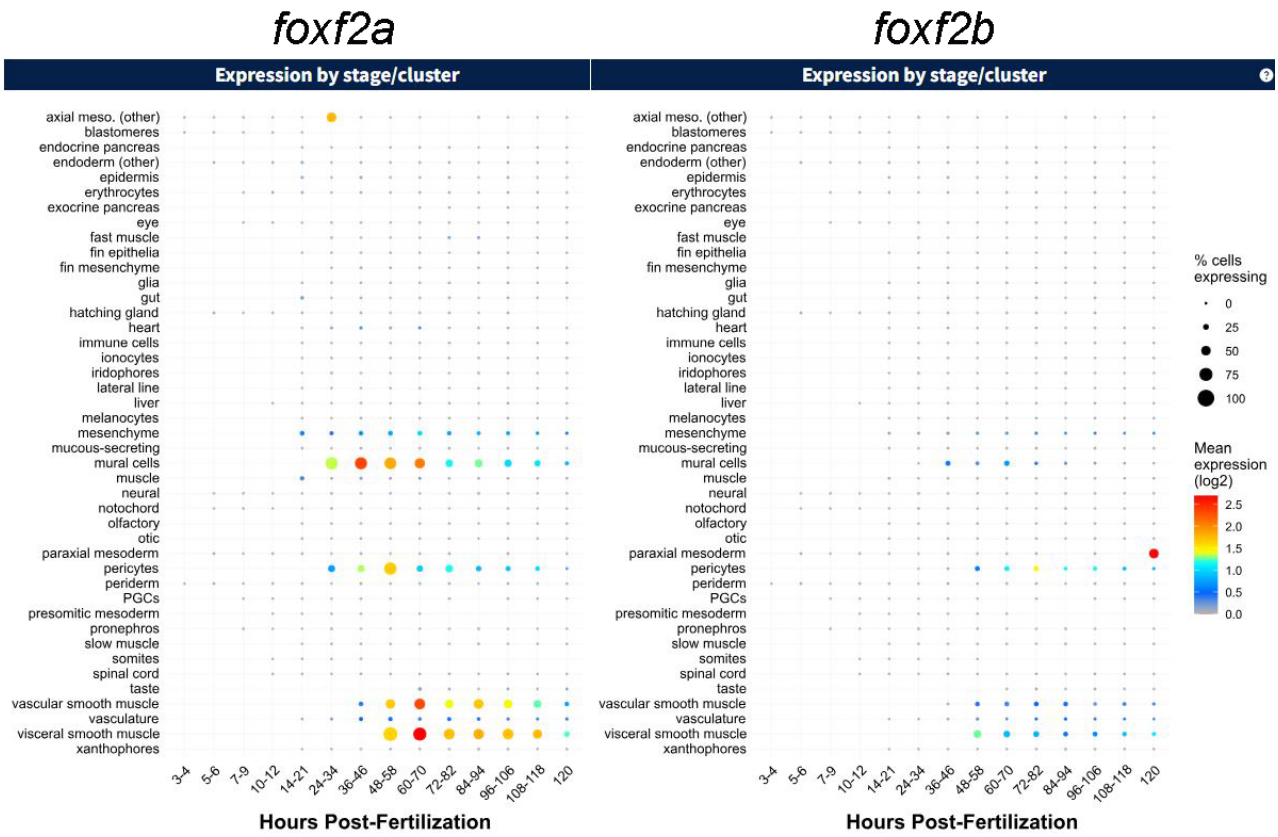

Supplemental Figure 4: Expression of *foxf2a* and *foxf2b* in single cell sequencing data from Daniocell. *foxf2a* is expressed strongly in mural cells, pericytes and smooth muscle (vascular and visceral), with lower expression of *foxf2b* in the same cell types. Available at: https://daniocell.nichd.nih.gov/.

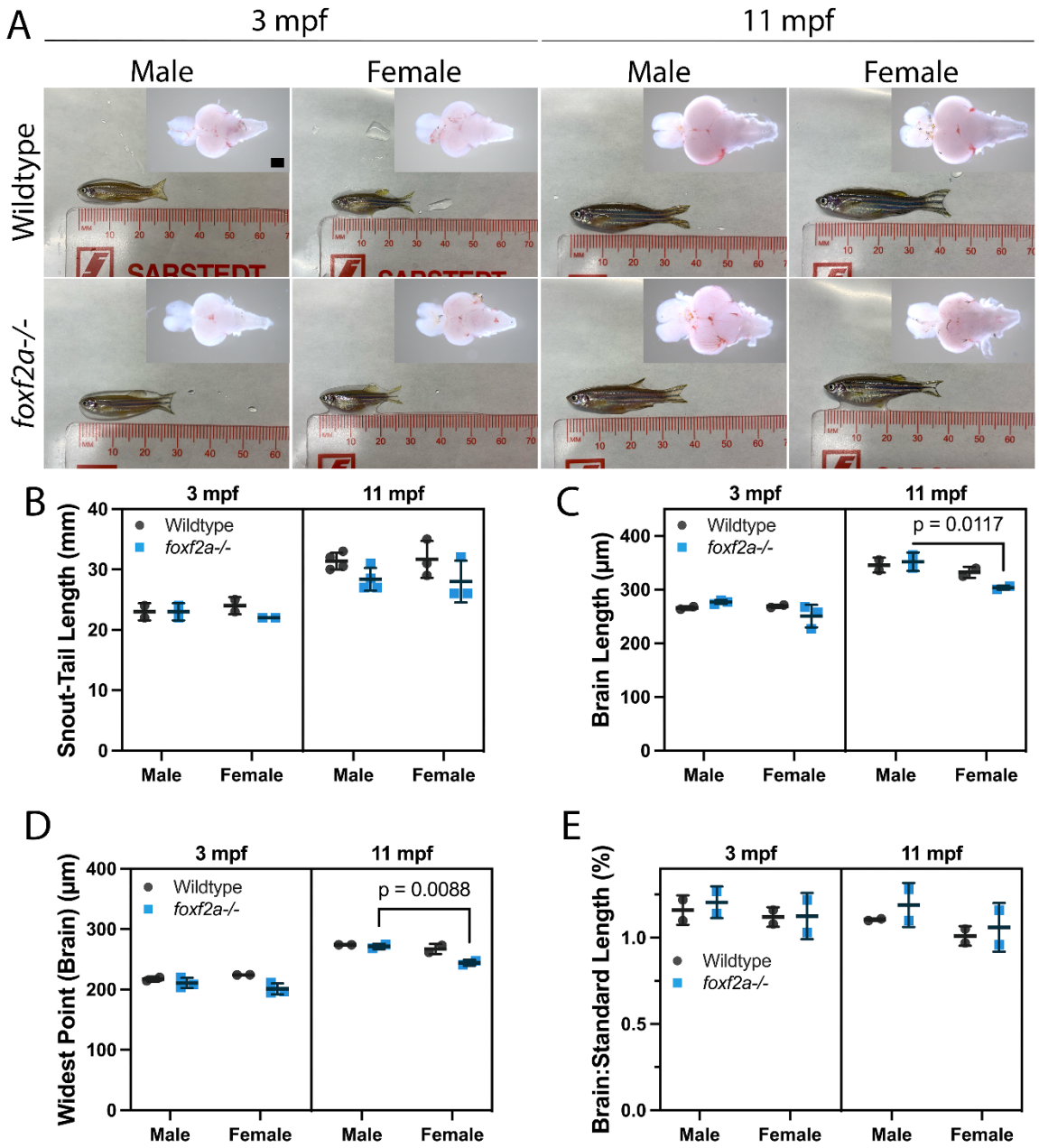

Supplemental Figure 5. *foxf2a mutant* adult brains have normal size as compared to wildtypes. (A) 3-month-old and 11-month-old *foxf2a*$^{-/-}$ mutant and wildtype brains were dissected and imaged dorsally under Brightfield. (B) Standard length measured from snout to base of the tail. (C) Brain length was measured from the tip of the forebrain to the end of the cerebellum. (D) Widest portion of midbrain measured. (E) Ratio of brain length relative to standard length. Statistical analysis was conducted using two-way ANOVAs with Šídák's multiple comparison test. Scale bars, 50 µm (A).

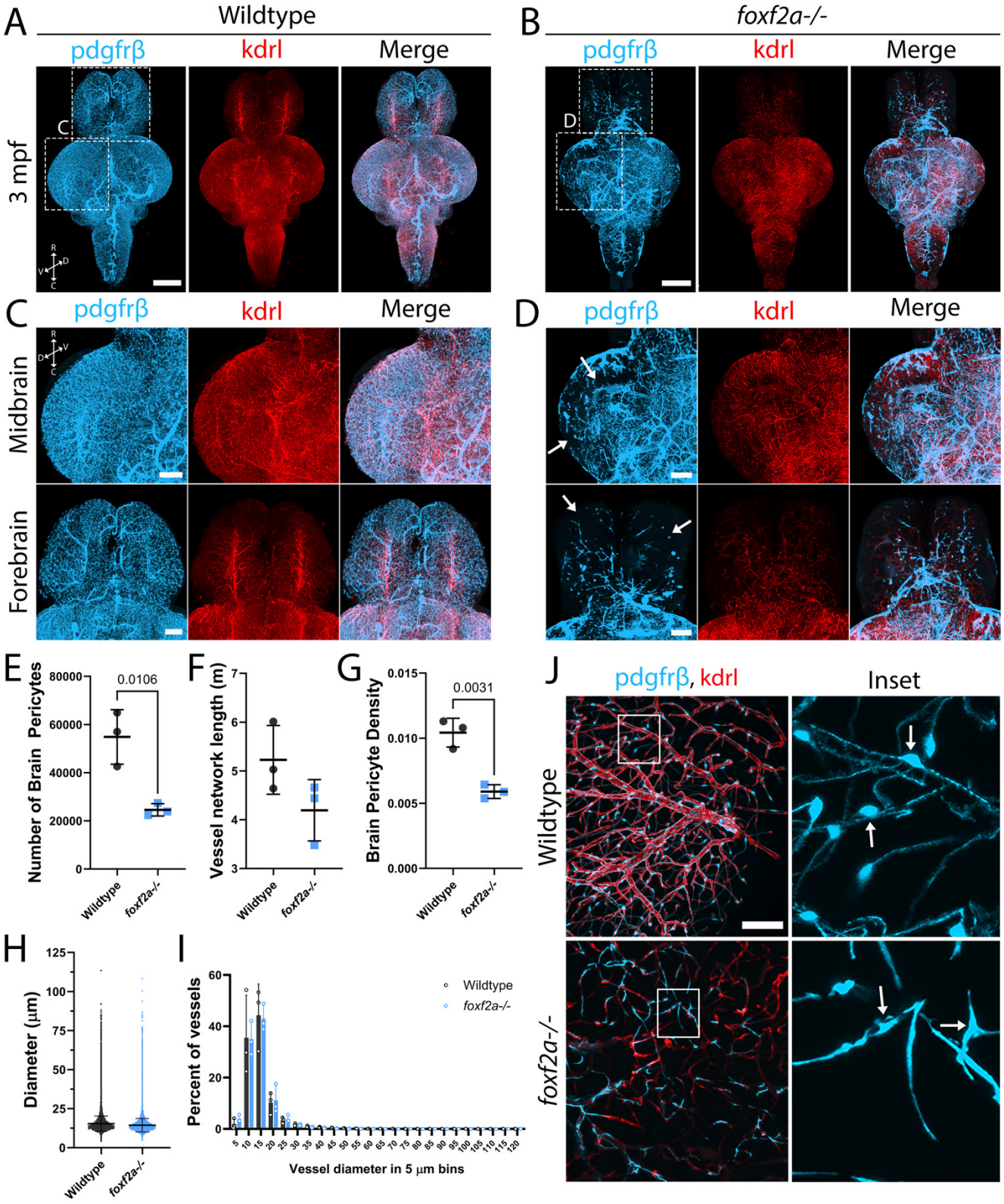

Figure 3. *foxf2a* mutants show strong brain vascular defects as adults. (A-B) 3D projections of iDISCO-cleared immunostained whole wildtype and *foxf2a*$^{-/-}$ brains at 3 mpf, viewed ventrally. (C-D) Wildtype and *foxf2a* mutant 2 brain regions, viewed dorsally (arrows = defects in coverage). (E) Number of brain pericytes in 3 individual wildtype and mutant brains at 3 mpf detected using Imaris' spot tool and machine learning. (F) Total vessel network length in 3 individual wildtype and mutant

brains at 3 mpf using Ilastik and Imaris' filament tool and machine learning. (G) Brain pericyte density calculated using number of brain pericytes per meter of vessel length. (H) Vessel diameter in 3 individual wildtype and mutant brains at 3 mpf using Imaris' filament tool and machine learning. (I) Percentage of vessel segments in wildtype and mutant brains at 3 mpf segregated by vessel diameter (in 5 µm bins). (J) CUBIC-cleared wildtype and *foxf2a* mutant midbrain at 11 mpf (arrows: individual pericyte soma). C = caudal, D = dorsal, R = rostral, V = ventral. Statistical analysis was conducted using unpaired t-tests (E-H) and Anova with Dunnett's post hoc test (I). Scale bars, 500 µm (A-B), 200 µm (C-D), 50 µm (J).

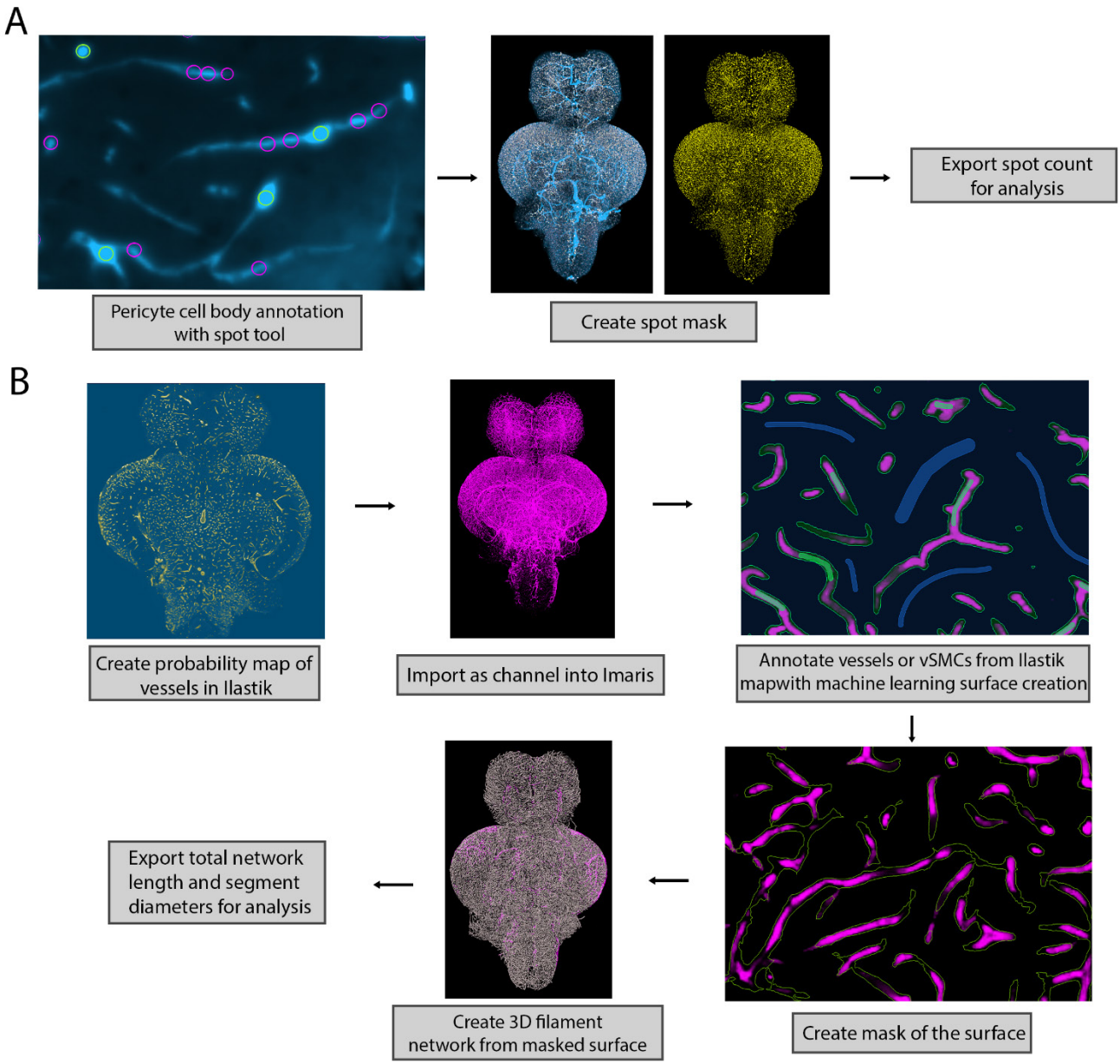

Supplemental Figure 6. Workflow of computational analysis of vascular network in adult brains. (A) Pericyte cell bodies annotated using the spot tool and machine learning in Imaris (green: cell bodies; purple: processes). A mask was created from the annotations, with each cell body annotated in yellow. The total number of cells was exported for statistical analysis. (B) Vessels were annotated in Ilastik to create a vessel probability map (yellow: blood vessels; blue: background). The map was imported as a channel into Imaris, where it would be further annotated with machine learning using the surface tool (green: blood vessels; blue: background). A mask was created from the surface, which was used to create a 3D network using the filament tool. Total network length and segment diameters were exported.

Movie 1. Rotating view of a cleared wildtype brain at 3 mpf with *pdgfr*β (blue) and *kdrl* (red).

Movie 2. Rotating view of a cleared *foxf2a* mutant brain at 3 mpf with *pdgfr*β (blue) and *kdrl* (red).

Movie 3. Rotating view of a cleared wildtype brain at 6 mpf with *acta2* (blue) and *kdrl* (red).

Movie 4. Rotating view of a cleared *foxf2a* mutant brain at 6 mpf with *acta2* (blue) and *kdrl* (red).

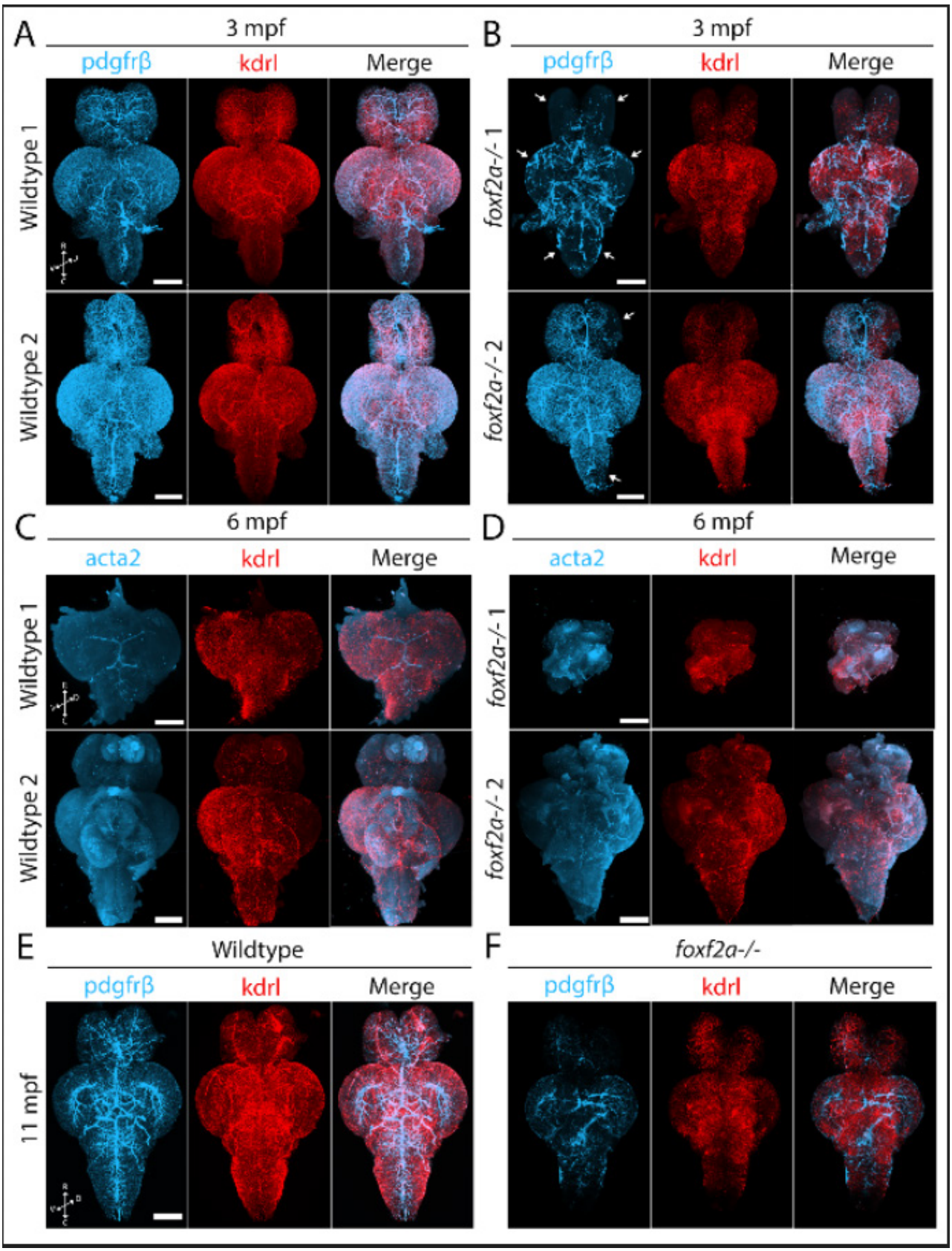

Supplemental Figure 7. *foxf2a* mutants show strong brain vascular defects in adulthood. (A-B) 3D projections of iDISCO-cleared immunostained whole wildtype and *foxf2a*$^{-/-}$ brains at 3 mpf with *Tg(pdgfrβ:Gal4, UAS:GFP, kdrl:mCherry)*, viewed ventrally (arrows = defects in coverage). (C-D) 3D

projections of iDISCO-cleared immunostained whole wildtype and *foxf2a*$^{-/-}$ brains at 6 mpf with *Tg(acta2:GFP, kdrl:mCherry)*, viewed ventrally (E-F) 3D projections of CUBIC-cleared whole wildtype and *foxf2a*$^{-/-}$ brains at 11 mpf with *Tg(pdgfrβ:Gal4, UAS:GFP, kdrl:mCherry)* viewed ventrally. R = rostral, C = caudal, D = dorsal, V = ventral. Scale bars, 500 μm (A-D), 700 μm (E-F).

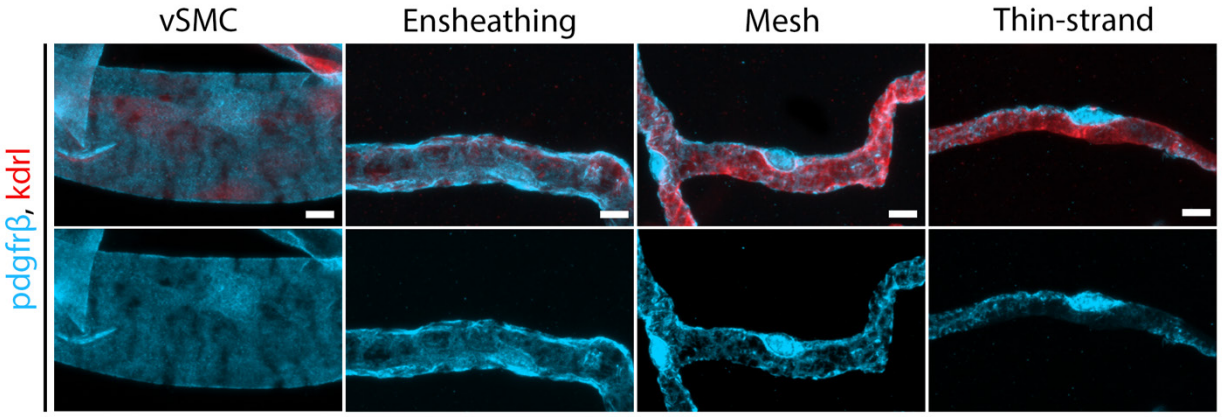

Supplemental Figure 8. Pericyte heterogeneity in the adult zebrafish brain. Immunolabeling for mural cell transgenes (*kdrl:mCherry and pdgfr*β*:Gal4, UAS:GFP*) on zebrafish brain vibratome sections. Vascular smooth muscle cells (vSMC), and pericyte (ensheathing, mesh and thin strand) subtypes are present in the adult zebrafish brain. Scale bars, 5 µm.

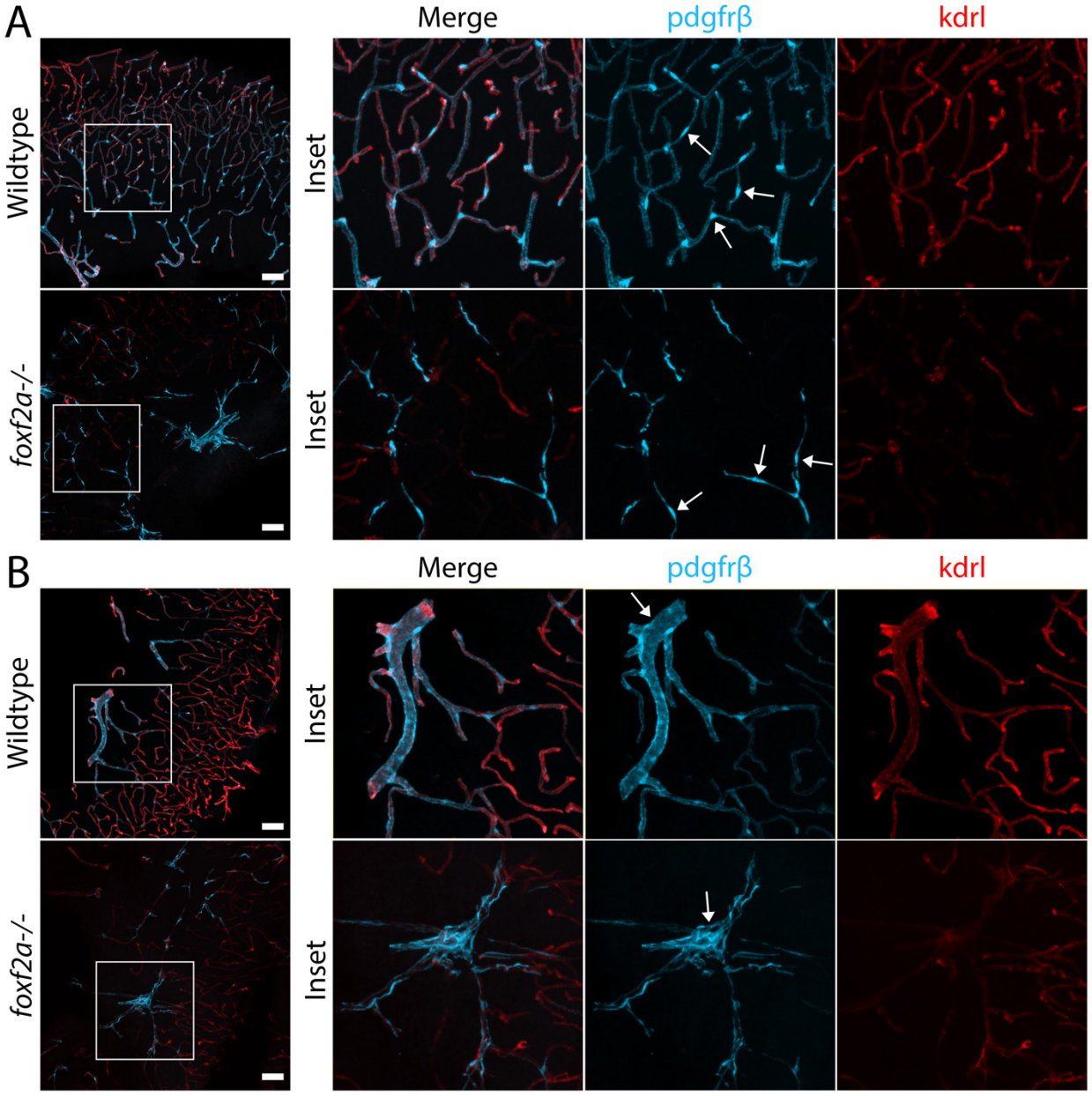

Supplemental Figure 9. *foxf2a* mutants show morphologically unusual *pdgfrβ*-expressing cells and blood vessels in the adult brain. Immunolabeled sections in equivalent regions of wildtype and *foxf2a*$^{-/-}$ mutant brains at 11 mpf. (A) Region of the brain with an inset of *pdgfrβ*-expressing mural cells, likely vSMCs (arrows: large calibre vessel). (B) Region of the brain with an inset of pericytes (arrows: individual cell bodies. Scale bars, 50 μm (A-B).

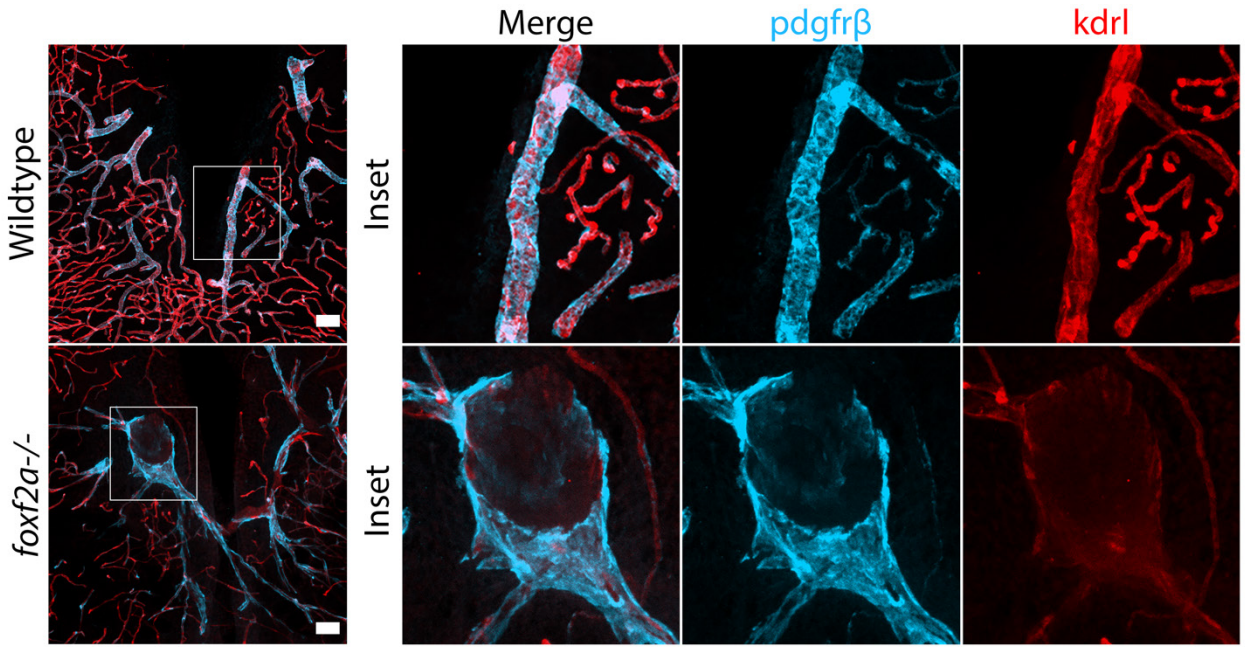

Supplemental Figure 10. Abnormal blood vessels become apparent in adult *foxf2a* mutant brains. Immunolabeled sections in equivalent regions of wildtype and *foxf2a*$^{-/-}$ mutant brains at 11 mpf. Large aneurysm-like structure with downregulated *kdrl* compared to the matched wildtype region. Scale bars, 50 μm (A-B).

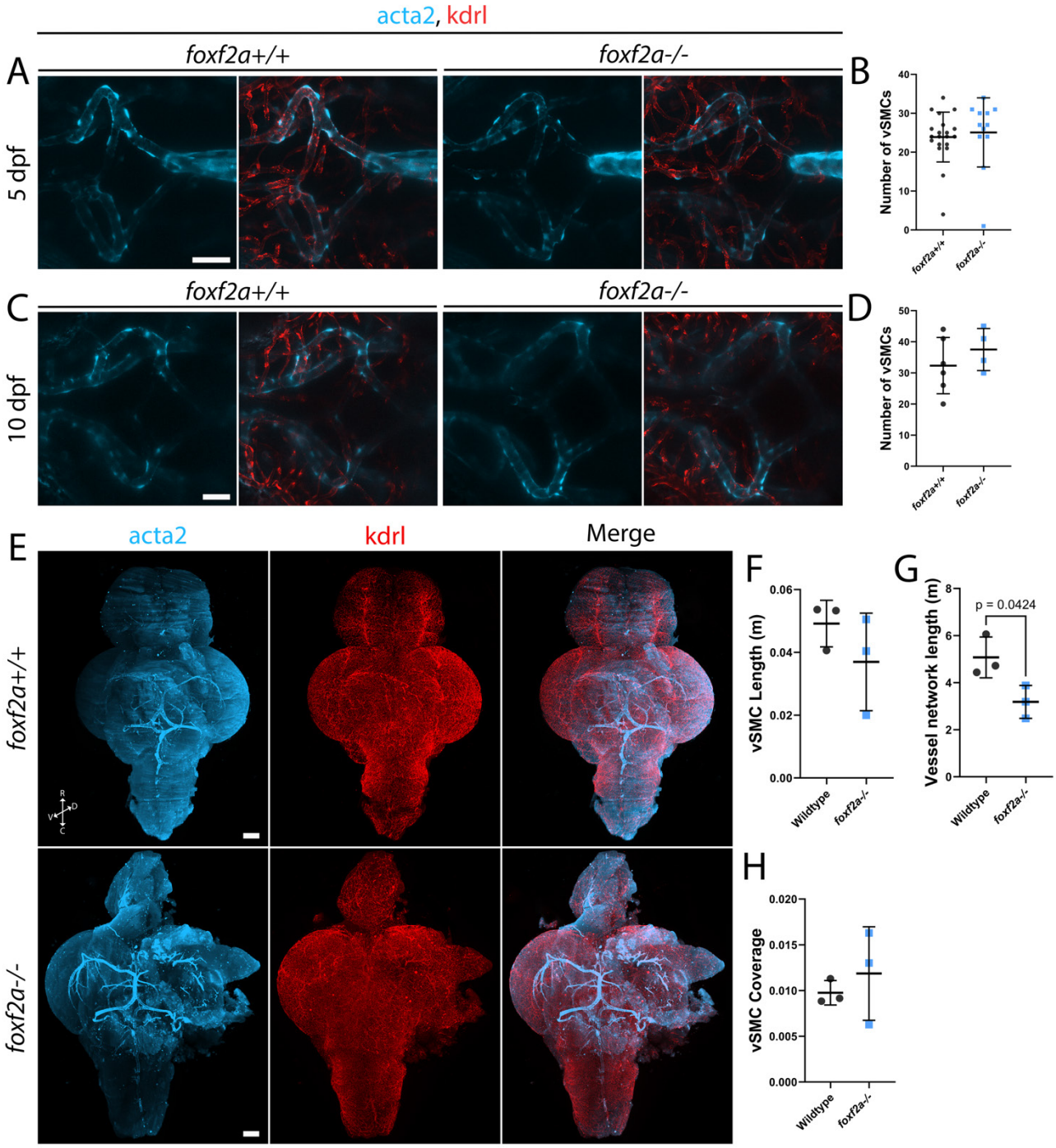

Figure 4. Loss of *foxf2a* has no impact on *acta2*-expressing brain vascular smooth muscle cells. (A) *foxf2a+/+* and *foxf2a-/-* larvae at 5 dpf showing vSMC coverage in the brain using endothelial (red; *Tg(kdrl:mCherry))* and vSMC (light blue; *Tg(acta2:GFP))* transgenic lines. (B) Scatter plot of total vSMCs at 5 dpf. (C) *foxf2a+/+* and *foxf2a-/-* larvae at 10 dpf showing vSMC coverage in the brain. (D) Scatter plot of total vSMCs at 10 dpf. (E) 3D projections of iDISCO-cleared immunostained whole wildtype and *foxf2a*$^{-/-}$ brains at 6 mpf, viewed ventrally. (F) Total vSMC length at 6 mpf using Imaris' filament tool and machine learning. (G) Total vessel network length at 6 mpf Ilastic and Imaris' filament tool and machine learning. (H) vSMC coverage per total blood vessel network length at 6 mpf. C = caudal, D = dorsal, R = rostral, V = ventral. Statistical analysis was conducted using unpaired t-tests. Scale bars, 20 µm (A, C), 200 µm (E).

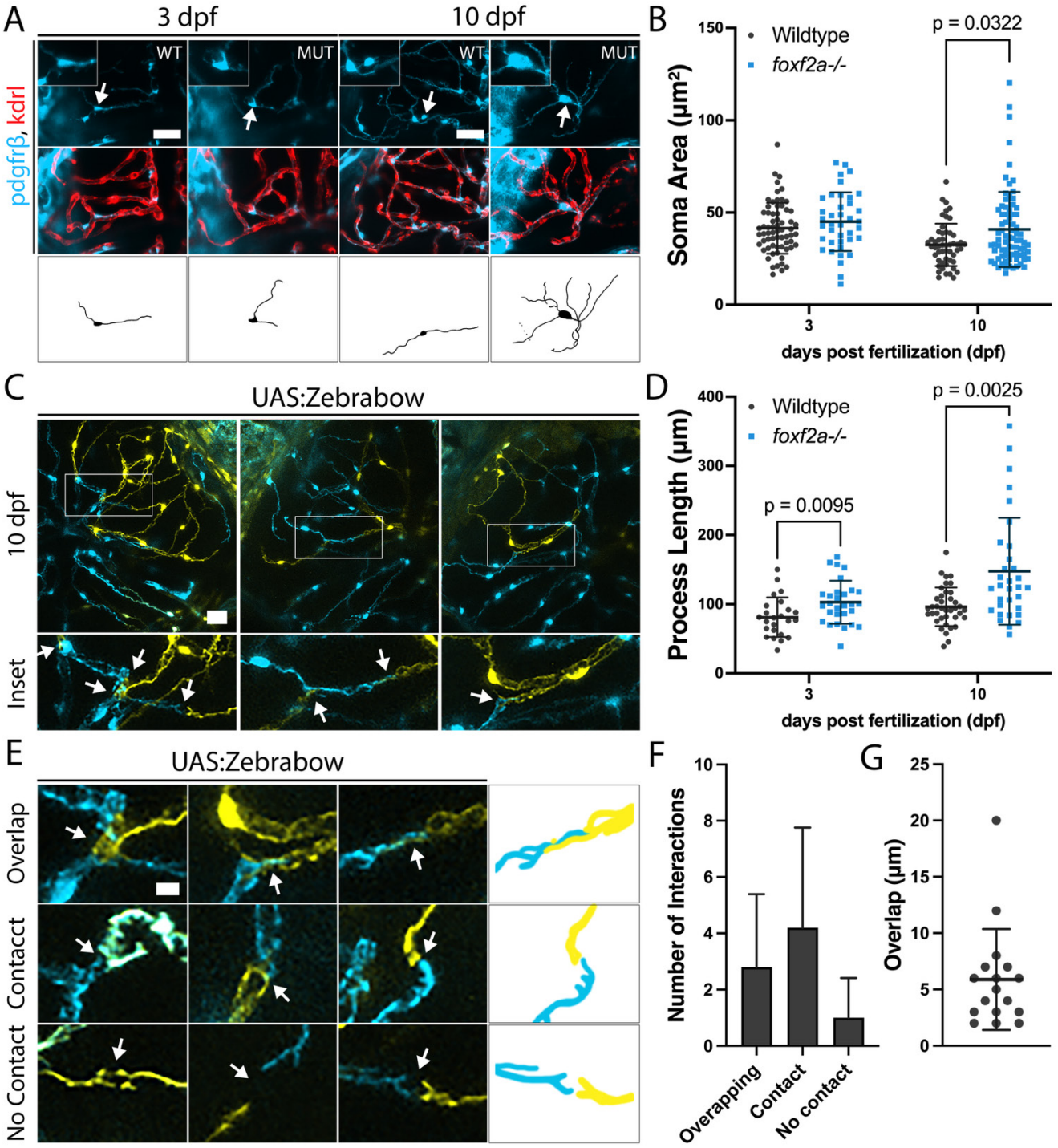

Figure 5. *foxf2a* mutant brain pericytes show increased soma size and process length. (A) Wildtype and *foxf2a*$^{-/-}$ mutant brain pericytes at 3 and 10 dpf with tracings of individual pericytes (indicated by arrows). (B) Brain pericyte soma area at 3 and 10 dpf. (C) Multispectral Zebrabow labelling reveals pericyte-process interactions in the larval brain. (arrows: pericyte interaction points). (D) Total process length per pericyte at 3 and 10 dpf. (E) Varying pericyte-pericyte interactions at 10 dpf (arrows: interaction points). (F) Number of each type of interaction at 10 dpf. (G) Length of overlap when process interaction occurs. Statistical analysis was conducted using multiple Mann-Whitney tests in B, a one-way ANOVA with Tukey's test at 3 dpf and a Kruskal-Wallis test with Dunn's multiple comparisons test at 10 dpf in D. Scale bars, 25 μm (A), 20 μm (C), 5 μm (E).

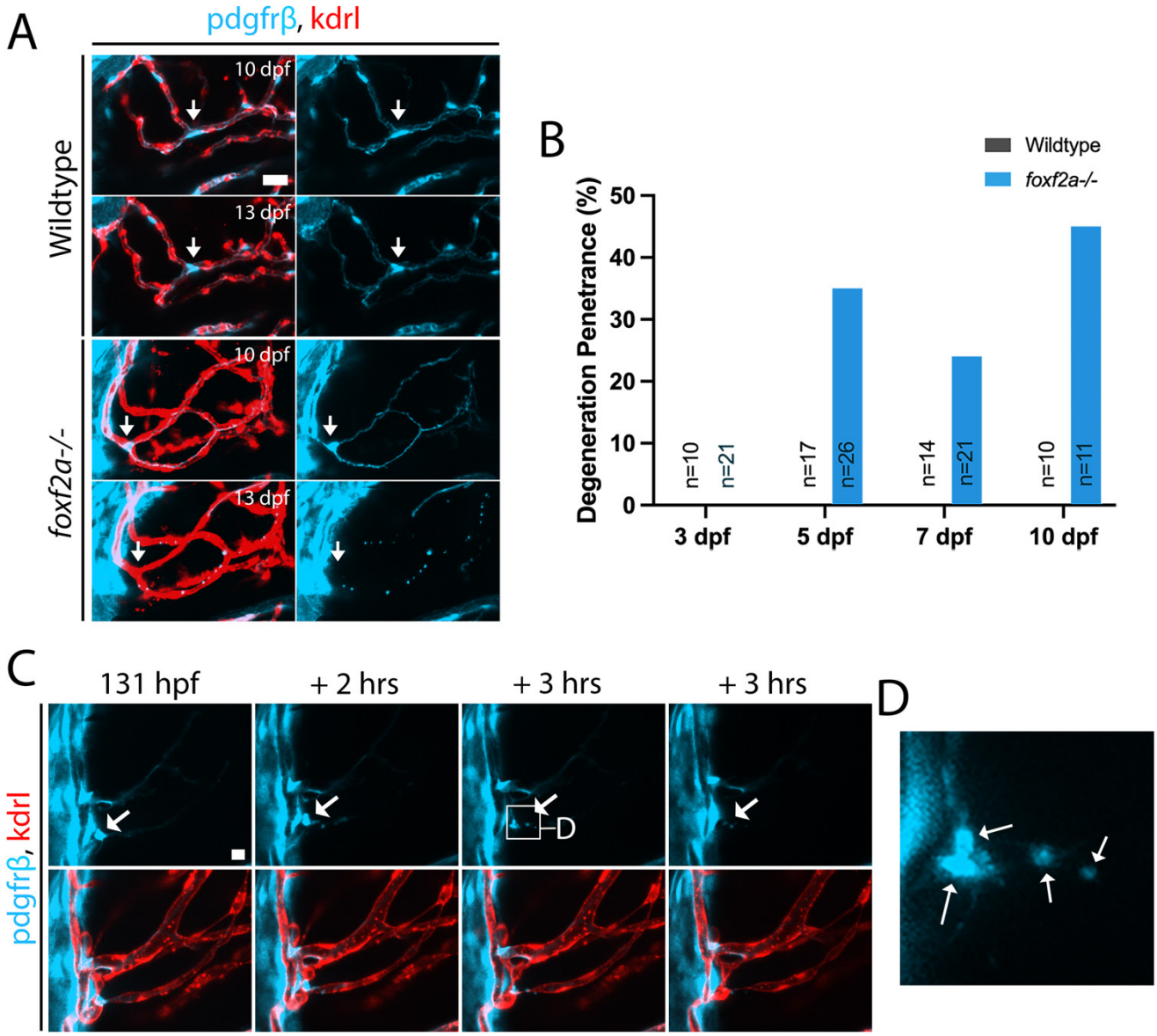

Figure 6. *foxf2a* mutant pericytes degenerate. (A) *foxf2a*$^{-/-}$ mutant pericyte at 10 and 13 dpf with the degenerating process and cell body with a wildtype control from the same brain region (arrows: individual pericyte). (B) Bar graph with process blebbing phenotype penetrance in wildtype and mutant brains (n = total samples examined). (C) Time-lapse of a *foxf2a*$^{-/-}$ mutant midbrain from 4-5 dpf (arrows: individual pericyte). (D) Inset of mutant pericyte undergoing degeneration (arrows: blebbing). Scale bars, 20 μm (A, C).

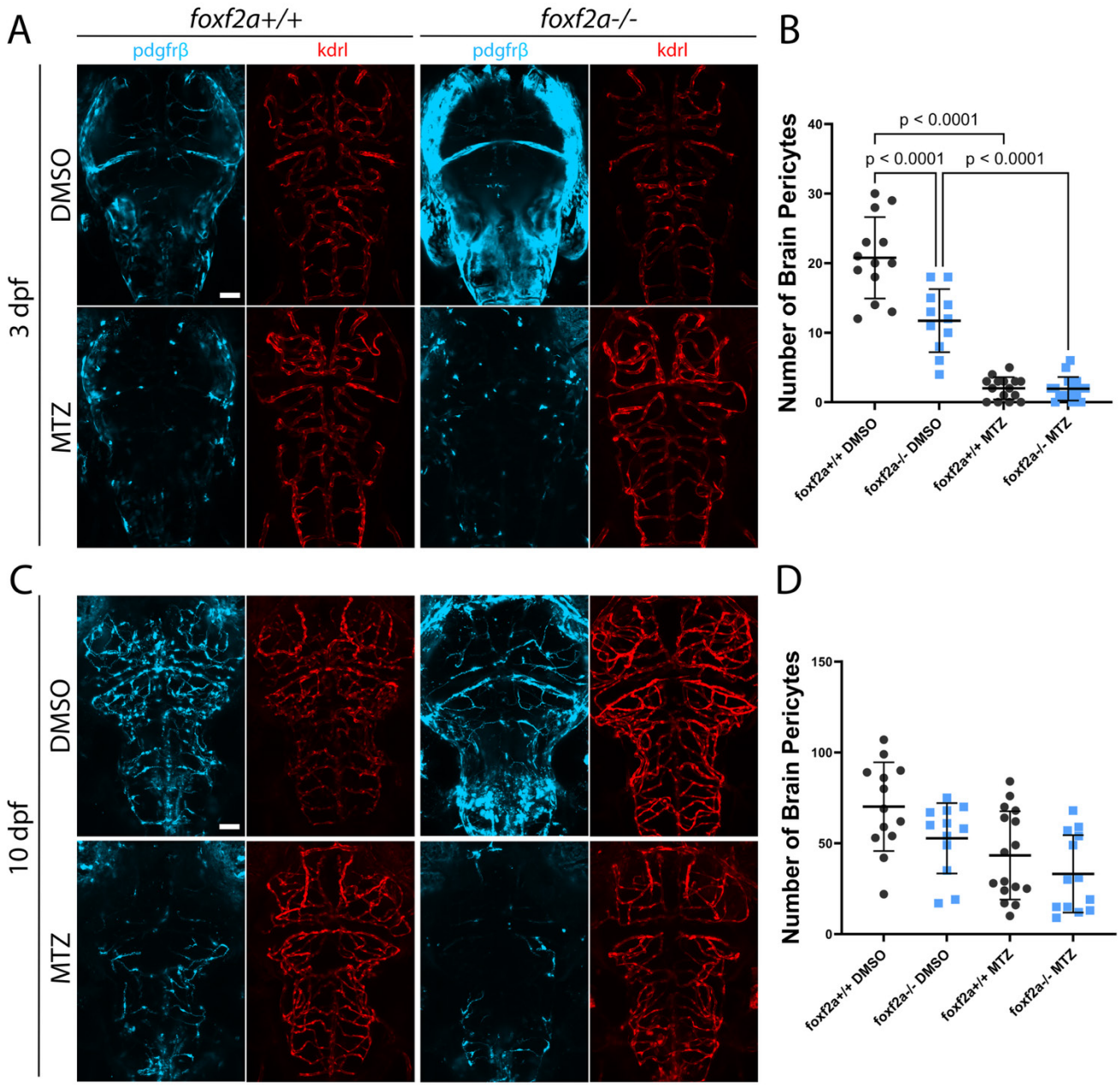

Figure 7. *foxf2a* mutants regenerate brain pericytes normally after genetic ablation. Zebrafish brains were imaged using endothelial (red; *Tg(kdrl:GFP)*) and pericyte (light blue; *Tg(pdgfrβ:Gal4, UAS:NTR-mCherry)*) transgenic lines. (A) Wildtype and mutant brains at 3 dpf in control (DMSO) and treated (MTZ) groups. (B) Total brain pericytes at 3 dpf. (C) Wildtype and mutant brains at 10 dpf. (D) Total brain pericytes at 10 dpf. Statistical analysis was conducted using a one-way ANOVA (B) or Kruskal-Wallis test with Dunn's multiple comparisons test (D). Scale bars, 50 μm (A, C).

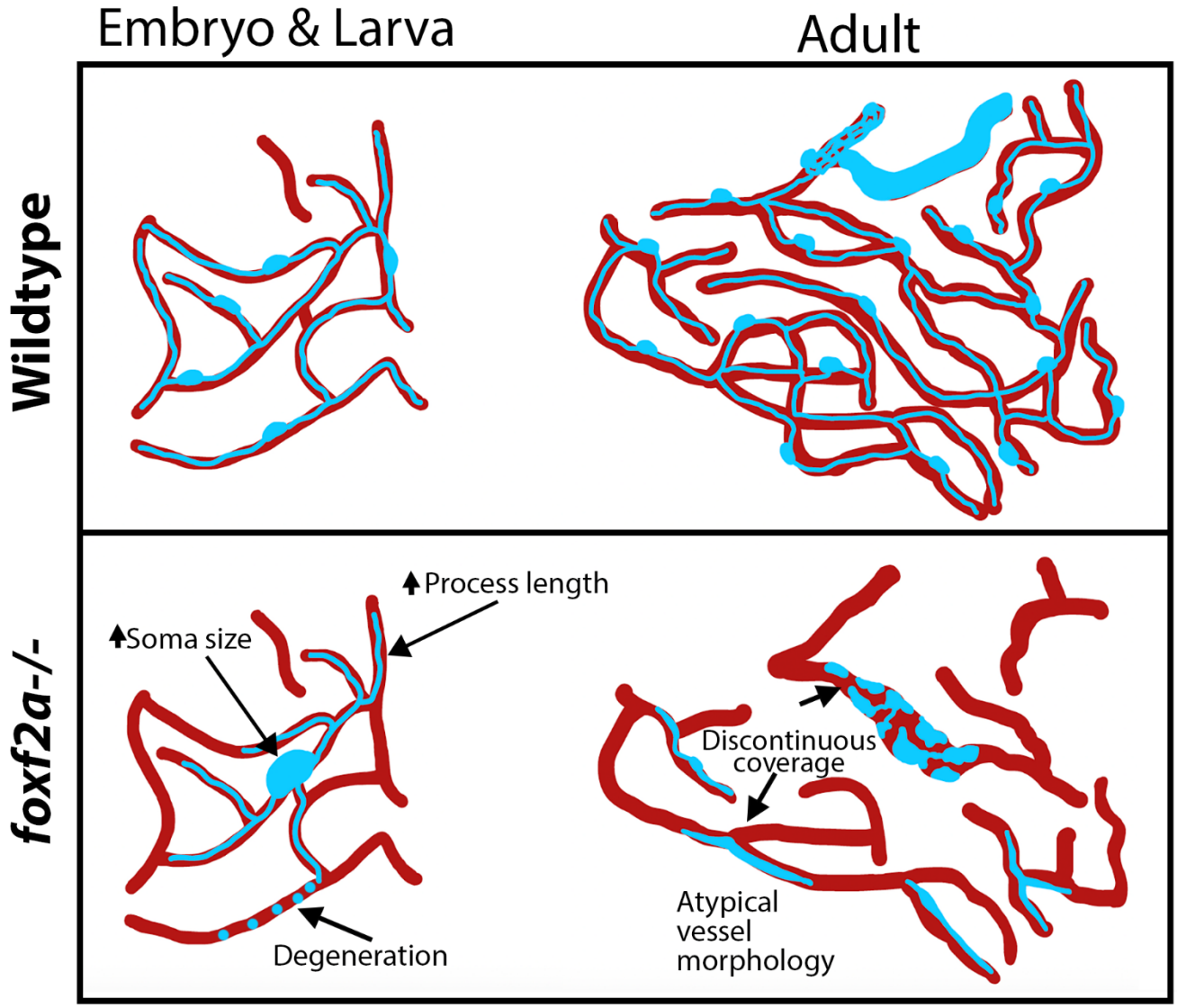

Figure 8. Model of *foxf2a* mutant brain pericyte defects over the lifespan. Wildtype pericytes develop normally in the embryo and establish extensive, continuous coverage over vessels by adulthood. *foxf2a* mutant pericytes exhibit abnormal morphology during development that worsens over the lifespan, with mutant vessels developing atypical morphology and discontinuous coverage.

Table 1: Key Resources Table

Reagent type (species) or resource	Designation	Source or reference	Identifiers
gene (D. Rerio)	foxf2a		ZDB-GENE-110407-5
gene (D. Rerio)	foxf2b		ZDB-GENE-041001-130
strain, strain background (D. Rerio)	*foxf2a*^{ca71}	Ryu et al., PNAS, 2022	ZDB-ALT-230214-10
strain, strain background (D. Rerio)	*foxf2b*^{ca22}	Chauhan et al., Lancet Neurology, 2016	ZDB-ALT-160809-1
strain, strain background (D. Rerio)	*Tg(acta2:GFP)*^{ca7}	Whitesell et al., Dev Bio, 2014	ZDB-ALT-120508-1
strain, strain background (D. Rerio)	*Tg(4xUAS:Zebrabow-B)*^{a133}	Pan et al., Devt, 2013	ZFIN: ZDB-ALT-130816-3
strain, strain background (D. Rerio)	*Tg(flk:GFP)*^{la116}	Choi et al., Devt, 2007	ZDB-TGCONSTRCT-070529-1
strain, strain background (D. Rerio)	*Tg(kdrl:mCherry)*^{ci5}	Proulx et al., Dev Bio, 2010	ZFIN: ZDB-ALT-110131-57
strain, strain background (D. Rerio)	*Tg(UAS:NTR-mCherry)*^{c264}	Davison et al., Dev Bio, 2007	ZDB-ALT-070316-1
strain, strain background (D. Rerio)	*TgBAC(4xUAS:EGFP)*^{mpn100Tg}	Demaria et al., Jneuro, 2013	ZFIN: ZDB-TGCONSTRCT-140812-1
strain, strain background (D. Rerio)	*TgBAC(pdgfrβ:GAL4FF)*^{ca42}	Whitesell et al., Dev Bio, 2019	ZFIN: ZDB-ALT-200102-2
strain, strain background (D. Rerio)	*TgBAC(pdgfrβ:EGFP)*^{ca41Tg}	Whitesell et al., Dev Bio, 2019	ZDB-TGCONSTRCT-160609-1
antibody	1/500 anti mCherry, rat monoclonal	ThermoFisher, M11217	RRID:AB_2536611
antibody	1/500 anti Green Fluorescent Protein, mouse monoclonal	Clontech, 3P 632380	RRID:AB_10013427
antibody	1/500 Donkey anti mouse 488	ThermoFisher, A-21202	RRID:AB_141607
antibody	1/500 Goat anti rat 555	ThermoFisher, A-21434	RRID:AB_2535855
commercial assay or kit	Fluoromount-G™ Mounting Medium with DAPI	Invitrogen	E141201
commercial assay or kit	Fluoromount-G™ Mounting Medium	ThermoFisher	00-4958-02
commercial assay or kit	Taqman SNP genotyping kit for foxf2b^{ca22}	Applied Biosystems	ANAACEC
commercial assay or kit	KAPA2G Fast Hotstart Genotyping Mix	Roche	KK5621
chemical compound, drug	Dimethylsulfoxide	Sigma	D8418
chemical compound, drug	Phenylthiourea	Sigma	P7629
chemical compound, drug	UltraPure Agarose	Invitrogen	16520-050
chemical compound, drug	Metronidazole	Sigma	M3761
software, algorithm	Imaris 10.3	Oxford Instruments	
software, algorithm	Ilastic	https://www.ilastik.org/	doi.org/10.1038/s41592-019-0582-9
software, algorithm	Fiji (ImageJ)	Schindelin et al., 2012	
software, algorithm	GraphPad Prism 10	Graphpad	
software, algorithm	Adobe Photoshop	Adobe	
software, algorithm	VesselMetrics	McGarry et al., Microvasc Res, 2024	doi.org/10.1016/j.mvr.2023.104610
commercial assay or kit	HCR™ Probe (v3.0) ndu4al2a	Molecular Instruments	
commercial assay or kit	HCR™ Probe (v3.0) kdrla	Molecular Instruments	
commercial assay or kit	HCR™ Probe (v3.0) pdgfrβ	Molecular Instruments	

commercial assay or kit	HCR™ Probe (v3.0) foxf2a	Molecular Instruments	
commercial assay or kit	HCR™ Probe (v3.0) foxf2b	Molecular Instruments	
sequence based reagent	foxf2a-genotyping-forward	IDT	ATG CAC TCG GCT CTC CAA AA
sequence based reagent	foxf2a-genotyping-reverse	IDT	GAT CGC CAT GAC TAT CGG GG

Table 2. Experimental N's and details used for figures.

Figure	Genotype	Age	# of Fish	
Figure 1C	Wildtype	3 dpf	10	
		5 dpf	17	
		7 dpf	10	
		10 dpf	10	
	foxf2a-/-	3 dpf	9	
		5 dpf	26	
		7 dpf	21	
		10 dpf	11	
Figure 1F	*foxf2a+/+*	3 dpf	7	
	foxf2a+/-		21	
	foxf2a-/-		8	
Figure S2B	Wildtype	3 dpf	3	
		5 dpf	3	
		7 dpf	3	
		10 dpf	2	
	foxf2a$^{-/-}$;foxf2b$^{-/-}$	3 dpf	5	
		5 dpf	5	
		7 dpf	5	
		10 dpf	4	
Figure	**Genotype**	**Age**	**# of Fish**	**# of Pericytes**
Figure S3A, 2D	Wildtype	72 hpf	**6**	37
	foxf2a-/-		**5**	14
Figure	**Genotype**	**Age**	**# of Fish**	**# of Pericytes**
Figure S3C, 2C	Wildtype	72 hpf	**4**	28
	Foxf2a-/-		**4**	9
Figure	**Genotype**	**Age**	**# of Fish per RNA extraction**	**# of Trials**
Figure 2E	Wildtype	48 hpf	50	4
	foxf2a-/-		50	4
Figure	**Genotype**	**Age**	**# of Fish**	**# of Vessel Segments**
Figure 2G, I, J	*foxf2a+/+*	3 dpf	7	N/A
	foxf2a+/-		21	
	foxf2a-/-		8	
Figure 2H	*foxf2a+/+*		7	72
	foxf2a+/-		21	93
	foxf2a-/-		8	87
Figure	**Genotype**	**Age**	**Sex**	**# of Fish**
Figure S4B	Wildtype	3 mpf	Male	2
			Female	2

		11 mpf	Male	4
			Female	3
	foxf2a$^{-/-}$	3 mpf	Male	2
			Female	2
		11 mpf	Male	4
			Female	3
Figure S4C-E	Wildtype	3 mpf	Male	2
			Female	2
		11 mpf	Male	2
			Female	2
	foxf2a$^{-/-}$	3 mpf	Male	3
			Female	3
		11 mpf	Male	2
			Female	2
Figure	**Genotype**	**Age**	**# of Fish**	
Figure 3E-G	Wildtype	3 mpf	3	
	foxf2a$^{-/-}$			
Figure	**Genotype**	**Age**	**# of Fish**	**# of Segments**
Figure 3H-I 3	Wildtype	3 mpf	3	522,029
	foxf2a$^{-/-}$		3	377,031
Figure	**Genotype**	**Age**	**# of Fish**	
Figure 4B	Wildtype	5 dpf	20	
	foxf2a$^{-/-}$		12	
Figure 4D	Wildtype	10 dpf	6	
	foxf2a$^{-/-}$		3	
Figure 4 F-H	Wildtype	6 mpf	3	
	foxf2a$^{-/-}$			
Figure	**Genotype**	**Age**	**# of Fish**	**# of Pericytes**
Figure 5B, D	Wildtype	3 dpf	6	66
		10 dpf	3	52
	foxf2a-/-	3 dpf	7	39
		10 dpf	11	77
	Wildtype$^{UAS:Zebrabow}$	3 dpf	6	24
		10 dpf	4	39
	foxf2a-/-	3 dpf	5	29
		10 dpf	5	32
Figure	**Genotype**	**Age**	**# of Fish**	
Figure 5F	Wildtype$^{UAS:Zebrabow}$	10 dpf	6	
Figure	**Genotype**	**Age**	**# of Fish**	**# of Interactions**
Figure 5G	Wildtype$^{UAS:Zebrabow}$	10 dpf	6	17
Figure	**Genotype**	**Age**	**# of Fish with Phenotype**	
Figure 6B	Wildtype	3 dpf	0/10	
		5 dpf	0/17	
		7 dpf	0/14	
		10 dpf	0/10	

	foxf2a-/-	3 dpf	0/21	
		5 dpf	9/26	
		7 dpf	5/21	
		10 dpf	5/11	
Figure	**Age**	**Genotype**	**Treatment**	**# of Fish**
Figure 7B	3 dpf	*foxf2a+/+*	DMSO	13
			MTZ	15
		foxf2a-/-	DMSO	11
			MTZ	16
Figure 7D	10 dpf	*foxf2a+/+*	DMSO	13
			MTZ	16
		foxf2a-/-	DMSO	12
			MTZ	13